

Cadmium Telluride Solar Cells

Brian E. McCandless¹ and James R. Sites²

¹University of Delaware, Newark, Delaware, USA, ²Colorado State University, Fort Collins, Colorado, USA

14.1 INTRODUCTION

Thin-film cadmium telluride (CdTe) solar cells are the basis of a significant technology with major commercial impact on solar energy production. Large-area monolithic thin-film modules demonstrate long-term stability, competitive performance, and the ability to attract production-scale capital investments. This chapter reviews the status of CdTe thin-film solar cells, with emphasis on the properties that make CdTe a favorable material for terrestrial photovoltaic solar energy conversion, their historical development, methods for device fabrication, analysis of device operation, and the fabrication strategies and technical challenges associated with present and future development of thin-film CdTe cells and modules.

Calculations of the dependence of ideal solar cell conversion efficiency on band gap show that CdTe is an excellent match to our sun, a G2 spectral-class star with an effective black-body photosphere surface temperature of 5700 K, and a total luminosity of 3.9×10^{33} erg/s. CdTe is a group II^B-VI^A compound semiconductor with a direct optical band gap that is nearly optimally matched to the solar spectrum for photovoltaic energy conversion. The direct band gap, $E_g = 1.5$ eV, and high absorption coefficient, $>5 \times 10^5/\text{cm}$, of CdTe means that high quantum yield can be expected over a wide wavelength range, from the ultraviolet to the CdTe band gap, $\lambda \sim 825$ nm. Short-wavelength photons, with energy greater than E_g , are absorbed near the CdTe surface, making CdTe an attractive absorber-layer material for thin-film solar cells. The theoretical solar cell efficiency versus band gap for CdTe and the optical absorption coefficient versus energy for CdTe and other selected photovoltaic materials are compared in Figure 14.1 [1, 2]. The high CdTe absorption coefficient, $>5 \times 10^5/\text{cm}$, for photons with $E > E_g$ translates into 99% absorption of the absorbable AM1.5 photons within 2 μm of film thickness.

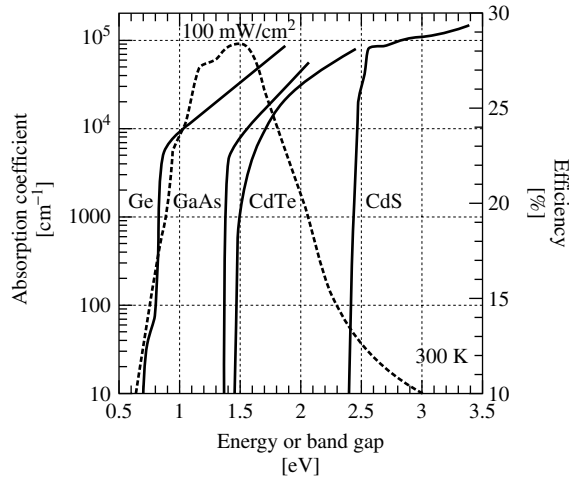


Figure 14.1 Theoretical solar cell efficiency (dotted) for AM1.5 spectral irradiance versus band gap and absorption coefficient (solid) versus energy for different semiconducting photovoltaic materials

CdTe emerged as a new electronic material in 1947 when Frerichs synthesized CdTe crystals by the reaction of Cd and Te vapors in a hydrogen atmosphere and measured their photoconductivity [3]. The early foundation for understanding the electronic nature of CdTe emerged from subsequent studies of single crystals purified by zone refinement. In 1954, Jenny and Bube [4] first reported that *p*-type and *n*-type conductivity could be obtained in CdTe by doping with foreign impurities. Shortly thereafter, Krüger and de Nobel [5] showed that the conductivity type could also be changed by varying the Cd–Te stoichiometry. Cd excess yields *n*-type and Te excess yields *p*-type conductivity, as had been discovered for PbS, PbSe, and PbTe. In 1959, the *p*–*T*–*x* diagram of the Cd–Te system and its relationship to intrinsic conduction and extrinsic conductivity via foreign-atom incorporation was established by de Nobel [6], who proposed the existence of two electronic levels associated with Cd vacancies and one with interstitial Cd to account for the measured changes in conductivity at different temperature and Cd partial pressure. Furthermore, the electronic levels associated with In as an *n*-type dopant and Au as a *p*-type dopant were estimated.

Loferski at RCA first proposed using CdTe for photovoltaic solar energy conversion in 1956 [1]. Although methods for controlling *n* and *p*-type conductivity in CdTe crystals were established by 1960, limited research was directed at the development of *p/n* homojunctions. In 1959, Rappaport, also at RCA, demonstrated single-crystal homojunction CdTe cells with conversion efficiency ~2% fabricated by diffusion of In into *p*-type CdTe crystals, yielding $V_{OC} = 600$ mV, $J_{SC} \sim 4.5$ mA/cm² (73 mW/cm² irradiance), and fill factor (*FF*) = 55% [7]. In 1979, the CNRS group in France achieved >7% conversion efficiency for a device made by close-space vapor transport deposition (VTD) of *p*-type arsenic-doped CdTe films onto *n*-type crystals, with $V_{OC} = 723$ mV, $J_{SC} \sim 12$ mA/cm² (AM1 irradiance) and *FF* = 63% [8]. Later they reported cells with efficiency >10.5%, with $V_{OC} = 820$ mV, $J_{SC} = 21$ mA/cm², and *FF* = 62% [9]. Little subsequent work on *p/n* CdTe homojunctions has been reported.

In contrast to p/n homojunction development, CdTe heterojunction solar cells have been widely investigated since 1960, proceeding along two paths, according to CdTe conductivity type. For n -type CdTe single crystals and polycrystalline films, extensive work was carried out on heterojunctions with p -type Cu_2Te . In the early 1960s, n -type CdTe/ p -type Cu_2Te devices having a structure analogous to the CdS/ Cu_2S solar cell [10] were fabricated, by surface reaction of n -type single crystals or polycrystalline films in acidic aqueous solutions containing Cu salts for topotaxial conversion of CdTe to p -type Cu_2Te [11–15]. By the early 1970s, the best thin-film CdTe/ Cu_2Te cells achieved cell efficiencies $>7\%$, with $V_{\text{OC}} = 550$ mV, $J_{\text{SC}} \sim 16$ mA/cm² (60 mW/cm² irradiance), and $FF = 50\%$, as reported by Justi *et al.* [16]. Interestingly, these cells utilized an underlying 5- μm -thick n -type CdS layer to improve adhesion and electrical contact of the 20- μm -thick CdTe film on molybdenum substrates. Difficulty in controlling the Cu_2Te formation process, poor device stability in CdTe/ Cu_2Te cells, and lack of a transparent p -type conductor ultimately shifted research emphasis to heterojunction structures employing p -type CdTe. Other work with n -type CdTe utilized Schottky barrier devices, formed by heating Pt or Au grids in contact with n -type CdTe single crystals [16] or electrodeposited CdTe thin films, with efficiencies approaching 9% [17].

For solar cells with single-crystal p -type CdTe, heterojunctions using stable oxides, such as $\text{In}_2\text{O}_3\text{:Sn}$ (ITO), ZnO, SnO_2 , and CdS have been more widely investigated. In these devices, the short wavelength spectral response is influenced primarily by the transmission of the heteropartner and low-resistance contact, collectively referred to as the window layer. Solar cells based on p -type CdTe single crystals with electron-beam-evaporated indium–tin oxide (ITO) window layers with efficiencies = 10.5% were developed by the Stanford group, 1977, with $V_{\text{OC}} = 810$ mV, $J_{\text{SC}} = 20$ mA/cm², and $FF = 65\%$ [18]. In 1987, cells made by the reactive deposition of indium oxide, In_2O_3 , on p -type CdTe single crystals yielded total area efficiencies = 13.4%, with $V_{\text{OC}} = 892$ mV, $J_{\text{SC}} = 20.1$ mA/cm², and $FF = 74.5\%$ [19]. In this device, the CdTe crystal had a carrier concentration of $6 \times 10^{15}/\text{cm}^3$ and the CdTe (111) face was etched in bromine methanol prior to loading into vacuum for In_2O_3 deposition. The V_{OC} of this cell remains the highest ever reported for a CdTe device. Solar cells with ZnO window layers on p -type CdTe single crystals yielded poorer junction behavior, with efficiency $<9\%$ and $V_{\text{OC}} = 540$ mV [20].

Cells made by evaporating n -type CdS films onto single-crystal p -type CdTe were first prepared by Muller *et al.* in the mid-1960s [21, 22], yielding conversion efficiencies less than 5%. In 1977, Mitchell *et al.* reported a conversion efficiency = 7.9% with $V_{\text{OC}} = 630$ mV for a cell with 1- μm -thick CdS and an ITO transparent electrode [23]. The highest efficiency for a cell fabricated with thin-film CdS on p -type CdTe single crystal was reported by Yamaguchi *et al.* in 1977. Their cell utilized 0.5- μm -thick CdS deposited by chemical vapor deposition onto the (111) face of phosphorous-doped CdTe single crystals and gave 11.7% efficiency with $V_{\text{OC}} = 670$ mV [24].

Thin-film CdTe/CdS heterojunction solar cells have been fabricated in two different configurations, referred to as *substrate* and *superstrate*. In both configurations, light enters the cell through the transparent conducting oxide (TCO) and CdS films. However, in the superstrate cell, the TCO, CdS, and CdTe layers are sequentially deposited onto a glass superstrate, which also serves as the mechanical support for the cell, and light must pass through the supporting glass before reaching the CdS/CdTe junction. In the substrate configuration, the CdTe film is typically deposited first onto a suitable

substrate, followed by sequential deposition of CdS and the TCO. Novel schemes have also been demonstrated for fabricating *substrate* configuration cells by transferring the entire cell from a disposable superstrate to a substrate (see, for example, Reference [25]). Superstrate polycrystalline CdTe/CdS heterojunction thin-film solar cells were first demonstrated in 1969 by Adirovich *et al.* in a superstrate design with evaporated CdTe on a CdS/SnO₂/glass superstrate, yielding an efficiency >2% [26]. This was followed in 1972 by Bonnet and Rabenhorst, who, in their paper for the 9th European Photovoltaic Specialists Conference, described a 5 to 6% efficient substrate design CdS/CdTe/Mo made by chemical vapor-deposited CdTe and vacuum-evaporated CdS films [27]. This paper delineated the fundamental issues that still influence the development of highly efficient CdTe/CdS thin-film solar cells: (1) the role of Cu in *p*-type doping of CdTe; (2) the controlling role of doping efficiency in CdTe; (3) the effects of abrupt versus graded CdTe–CdS junctions; (4) the effects of active versus passive grain boundaries; and (5) the formation of low-resistance contacts to *p*-type CdTe.

Development of thin-film CdTe/CdS solar cell fabrication processes during the 1980s and 1990s was advanced by refinements in device design, postdeposition treatments, and formation of low-resistance contacts rather than by refinements in specific deposition methods. This is primarily due to the relatively high chemical stability of CdTe compared to the elemental and compound precursors used to prepare it. Thus, numerous film-fabrication techniques have been used to deposit CdTe for moderate- to high-efficiency solar cells, and eight of these are reviewed in this chapter. Surprisingly, CdTe/CdS solar cells having conversion efficiency from ~10 to ~16% have similar photovoltaic behavior. Electrical analysis suggests that device operation is primarily limited by Shockley–Read–Hall recombination in the space charge region [28].

In spite of tolerance to the deposition technique, two enigmatic aspects of processing high-efficiency thin-film CdTe/CdS solar cells persist, that is, the use of superstrate device configuration, with CdTe deposited onto CdS, and the need for processing step(s) that expose the CdTe and CdS films to Cl and O. During the 1980s, significant gains in performance were obtained by empirical optimization of superstrate fabrication processes with respect to processing variables such as the CdTe deposition temperature, postdeposition heat treatment, growth or treatment chemical environment, and CdTe contact formation. For example, the Matsushita Battery Industrial Company reported that for screen-print/sintered CdTe cells, it was critical to control the CdCl₂, O, and Cu concentrations in the structure by adjusting the slurries and the temperature–time sequences of the sintering step [29]. The Monosolar electrodeposition process was optimized to the 10% efficiency level by addition of Cl to the CdTe plating bath and the use of a so-called “type-conversion junction formation” postdeposition treatment to electrically activate the cell [30]. The group at Kodak achieved the 10% efficiency level with close-space sublimation-deposited CdTe by optimizing the CdTe deposition temperature and the oxygen content in the deposition ambient [31]. A turning point for thin-film CdTe cell performance, with a collateral benefit for processing tolerance, was the application of a postdeposition air-heat treatment of CdTe/CdS structures coated with CdCl₂ [32, 33]. Combining the “CdCl₂ treatment” with advancements in low-resistance contact formation led to the achievement in 1993 of a >15% efficient cell with CdTe deposited by close-space sublimation [34]. Refinements in window-layer processing [35] and employing vapor CdCl₂ treatments [36] have led to additional improvements. The record efficiency

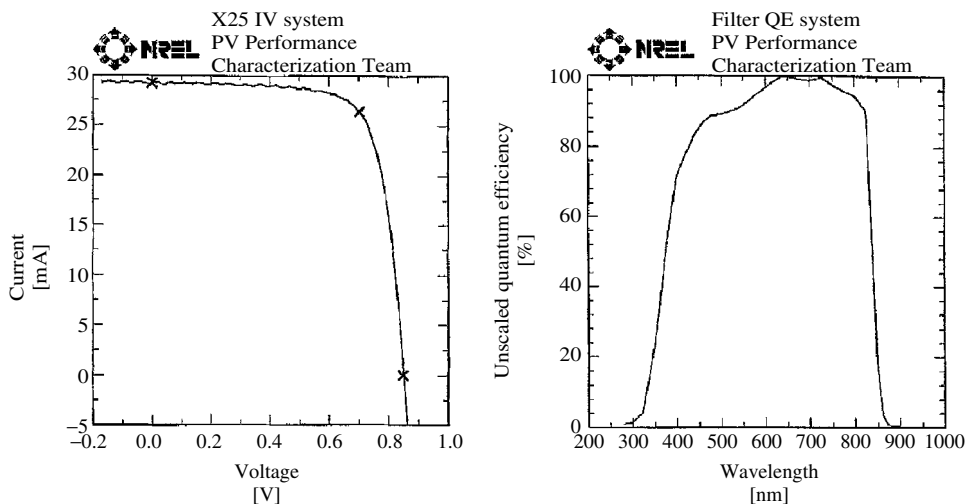


Figure 14.2 Current–voltage and relative quantum efficiency curves for 16.4%-efficient CdTe/CdS thin-film solar cell [37]

to date is 16.5% with $V_{OC} = 845$ mV, $J_{SC} = 25.9$ mA/cm², and $FF = 75.5\%$ [37]. The $J-V$ and quantum efficiency (QE) characteristics of this cell are shown in Figure 14.2.

Superstrate polycrystalline thin-film CdTe/CdS solar cells have received significant R&D attention and have achieved the highest performance among CdTe-based solar cell configurations. Consideration of the cell parameters obtained by devices in all configurations suggests that $V_{OC} = 900$ mV, $J_{SC} = 26$ mA/cm², and $FF = 80\%$, and efficiency approaching 19% are reasonable expectations without major breakthroughs. Translating high-efficiency cells to high-efficiency module fabrication, however, will require the additional understanding of processing tolerances, the effects of thermal and chemical nonuniformities in processing large-area devices, and the effects of cell-area delineation, interconnections, and encapsulants.

14.2 CdTe PROPERTIES AND THIN-FILM FABRICATION METHODS

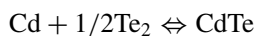
This section summarizes the fundamental properties of CdTe and describes methods for depositing polycrystalline CdTe thin films. CdTe is unique among the II^B-VI^A compounds, such as ZnS, CdSe, and HgTe, in that it exhibits the highest average atomic number, the least negative formation enthalpy, the lowest melt temperature, the largest lattice parameter, and the highest ionicity. Electronically, CdTe exhibits amphoteric semiconducting behavior, making it possible to intrinsically and extrinsically dope CdTe n and p -type. All these factors complement its nearly ideal optical band gap and absorption coefficient for terrestrial photovoltaic devices, making it a forgiving material to deposit and control in the thin-film form. Table 14.1 presents pertinent physical and optoelectronic data for CdTe.

The synthesis of II^B-VI^A compounds is facilitated by the large negative formation enthalpies (ΔH_f) and correspondingly low vapor pressures (p_{sat}) of the compounds compared to their constituent elements: for CdTe, $\Delta H_f = -22.4$ kcal/mol and $p_{sat}(400^\circ\text{C}) =$

Table 14.1 CdTe optoelectronic and physiochemical properties

Property	Value or range	Reference
Optical band gap; E_g (300 K)	1.50 eV \pm 0.01 eV	Single crystal [38] polycrystalline film [39]
Temperature dep: dE_g/dT	-1.7 meV/K	[40]
Electron affinity: χ_e	4.28 eV	[41]
Absorption coefficient (600 nm)	$6 \times 10^4/\text{cm}$	[38, 39]
Index refraction: (600 nm)	~ 3	[42]
Static Dielectric constant: $\varepsilon(\theta)$	9.4, 10.0	[41, 43]
High Freq. Dielectric constant: $\varepsilon(\infty)$	7.1	[43]
m_e^*	0.096	[44]
m_h^*	0.35	[44]
μ_e	500–1000	[44]
μ_h	50–80	[44]
Space group	F-43 m	[45]
Lattice parameter: a_0 (300 K)	6.481 Å	[45]
Cd–Te bond length	2.806 Å	Calculated from a_0
Density	~ 5.3	[42]
Heat of fusion: ΔH_f° (300 K)	-24 kcal/mol	[46]
Entropy: S° (300 K)	23 cal/deg-mol	[46]
Sublimation reaction	$\text{CdTe} \rightarrow \text{Cd} + 1/2\text{Te}_2$	[46]
Sublimation pressure: p_{sat}	$\log(P_s/\text{bar}) = -10\,650/T(\text{K}) - 2.56 \log(T) + 15.80$	[46]
Melting point	1365 K	[44]

10^{-5} Torr and for CdS, $\Delta H_f = -30$ kcal/mol and $p_{\text{sat}}(400^\circ\text{C}) = 10^{-7}$ Torr [46]. The equilibrium reaction for CdTe solid and Cd and Te vapors is



The CdTe temperature versus composition, T - x , atmospheric pressure phase diagram is shown in Figure 14.3(a). The individual vapor–solid equilibria for CdTe, CdS, Cd, Te, and CdCl_2 are shown in Figure 14.3(b) over the temperature range employed for fabricating solar cells, from 100 to 600°C . Congruent evaporation of CdTe facilitates vapor-deposition techniques, and the comparatively high sublimation pressures for Cd and Te ensure single-phase composition in deposits formed in vacuum at temperatures above $\sim 300^\circ\text{C}$. CdTe is also the stable product of cathodic reduction from solutions containing Cd and Te ions due to the reasonably close reduction potentials for Cd and Te and the low solubility product of CdTe.

The T - x phase equilibrium of the CdTe system at atmospheric pressure is characterized by Cd ($x = 0$) and Te ($x = 1$) endpoints and by the compound CdTe (Figure 14.3a). Note that the CdTe melt temperature, $T_m = 1092^\circ\text{C}$, is significantly higher than for either

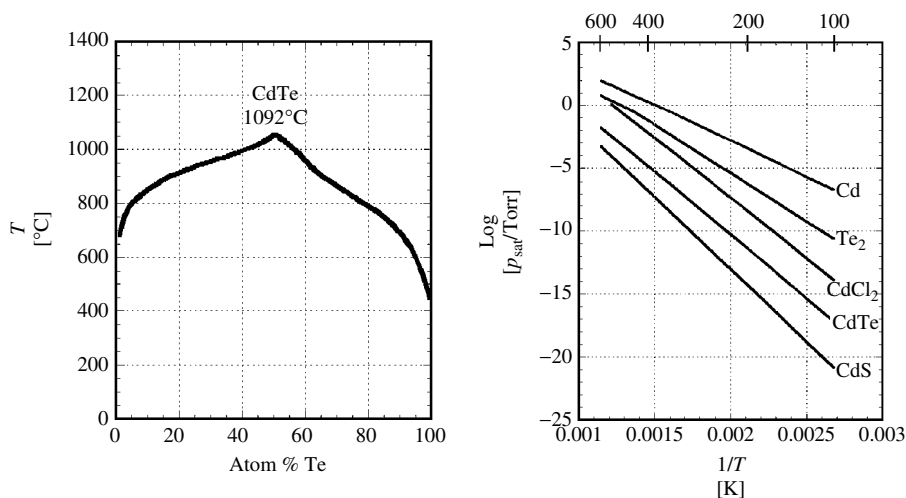


Figure 14.3 (a) CdTe T - x phase diagram (1 atm) [47] and (b) vapor–solid p_{sat} versus $1/T$ diagram for CdTe, CdS, CdCl_2 , Cd, and Te [48]

Cd, $T_m = 321^{\circ}\text{C}$, or Te, $T_m = 450^{\circ}\text{C}$ [49]. A detailed examination of the T - x projection around the CdTe stoichiometric composition indicates a very narrow, $\sim 10^{-6}$ at.%, symmetrical existence region at $T < 500^{\circ}\text{C}$. At higher temperatures, the existence region widens and is asymmetrical on the Cd-rich side up to 700°C and becomes Te-rich at higher temperatures [44]. The existence region and intrinsic defect structure are related by the preparation conditions of the bulk material and have been the subject of intensive investigation from the time since de Nobel [50]. Krüger published a comprehensive review of the defect chemistry in 1977 [51], and recently, theoretical treatments of defect levels in CdTe have extended this basis [52]. A critical topic of study is how the bulk properties transfer to thin-film CdTe.

The solid-state properties of CdTe are derived from the ionic character of the CdTe bond. Among the $\text{II}^{\text{B}}\text{-VI}^{\text{A}}$ compounds, CdTe has the highest value on the Phillips ionicity scale = 0.717, which is below the Phillips' threshold value of 0.785 for octahedral coordination [53]. Geometrical considerations show that tetrahedral coordination is favored in ionic binary compounds having cation/anion radius ratio between 0.225 and 0.732, while octahedral coordination is favored for a ratio greater than 0.732 [54]. In CdTe, the cation/anion radius ratio is $r(\text{Cd}^{2+})/r(\text{Te}^{2-}) = 0.444$, thus favoring tetrahedral coordination.

Tetrahedral atomic coordination, with the four nearest neighbors of the other element and the twelve next-nearest neighbors, leads to diamond structure in monatomic solids and zincblende and wurtzite structures in binary solids. Solid CdTe at atmospheric pressure exists in a face-centered cubic zincblende structure with unit cell dimension of 6.481 \AA and CdTe bond length of 2.806 \AA . Figure 14.4 depicts two views of the CdTe zincblende structure viewed across the closest-packing (111) plane, with alternating anion and cation planes, and viewed across the (110) plane, with equal numbers of anions and cations in each plane. These are the predominant orientations encountered in CdTe thin films.

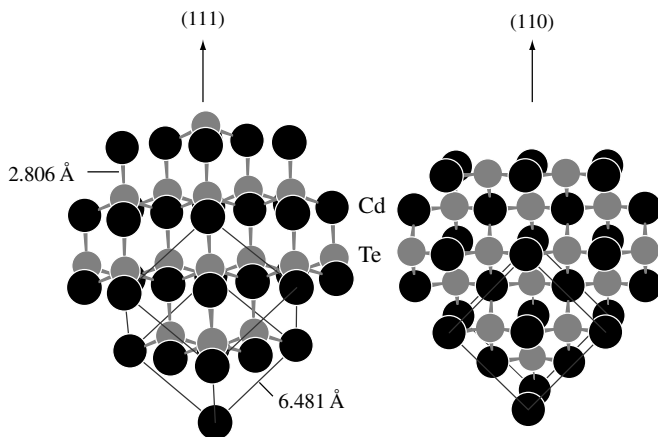


Figure 14.4 Zincblende CdTe crystal structure showing orientation with respect to (111) and (110) planes. The Cd atoms are black and Te atoms are gray. The Cd–Te bonds and F.C.C. unit cells are indicated for each view

CdTe polytypes are also known, depending on the formation pressure [55]. The hexagonal wurtzite structure, typically associated with tetrahedral coordination in predominantly covalent solids, is found in CdTe deposited in vacuum. No pure wurtzite bulk specimens have ever been reported [56]. Octagonal coordination, leading to the halite NaCl structure can be induced in CdTe by subjecting single crystals to high pressure, above 35 kbar. Among II–VI compounds, only CdO, with ionicity = 0.785, occurs with the halite structure at standard pressure and temperature.

The bulk optical and electronic properties of CdTe arise from the electronic-band structure within the periodic lattice near the valence-band maximum (VBM) and the conduction-band minimum (CBM). The VBM and CBM occur at the same momentum position, Γ , within the first Brillouin zone, giving rise to a direct band gap of 1.5 eV at 300 K. The temperature variation of the CdTe band gap is ~ -1.7 meV/K. The band curvature about the extrema represents the effective mass of electrons at the CBM and of holes at the VBM and controls carrier-transport properties and interband density-of-states (see Table 14.1).

Qualitatively, the band structure of CdTe can be understood from its relatively high ionicity, since the parts of the Bloch functions having the same periodicity as the lattice are related to the Cd and Te atomic orbitals. The conduction band arises from the first unoccupied level of the cation, namely, the 5s level of Cd. The uppermost valence band consists of the highest occupied level of the anion, namely, the 5p level of Te. It has been shown that cation d and anion p coupling reduce valence-band offsets in CdTe [57]. Detailed calculations of the E – k band structures in cubic CdTe and other II–VI compounds were originally carried out by the local pseudopotential method in the mid-1960s [58] and more recently using the linearized augmented plane-wave method, considering all electrons and relativistic kinematics [59].

Deviations from perfect single crystals cause profound changes in electronic and optical properties. Imperfections or defects disrupt the periodic structure, producing

localized electronic states within the band gap, E_g . It is customary to refer to states having ionization energy $\sim E_g/2$ as “deep” and states having ionization energy near the bands as “shallow.” The types of defects controlling electronic properties include native defects, chemical impurities, and complexes thereof; native defects and impurities can occur substitutionally or interstitially. For example, cadmium vacancy, V_{Cd} , gives rise to shallow acceptor states, while cadmium substitution on a tellurium site, Cd_{Te} , gives rise to shallow acceptor states. Interstitial cadmium, Cd_i , gives rise to a relatively shallow donor state, while tellurium, Te_i , gives rise to deep states. A selected group of native, impurity, and complex defect levels in CdTe is shown in Figure 14.5.

Present-generation high-efficiency CdTe solar cells are based on p -type CdTe and n -type CdS. The desired electrical properties are obtained by activation treatments that incorporate specific impurities into the CdTe and CdS layers such as postdeposition treatments that introduce $CdCl_2$, O_2 , and Cu into CdTe, which may activate or passivate native defects [61]. The specific effects of these agents on grain surfaces and the intragrain bulk properties must be considered separately to account for the enhanced p -type conductivity and the electrical passivation of grain boundaries in films after treatment. A comprehensive review of bulk diffusivities of group I, II, and III impurities in CdTe is given in Reference [62].

The polycrystalline aspect of cell fabrication gives rise to critical challenges for the development of *thin-film* photovoltaics: (1) separating intragrain from grain-boundary

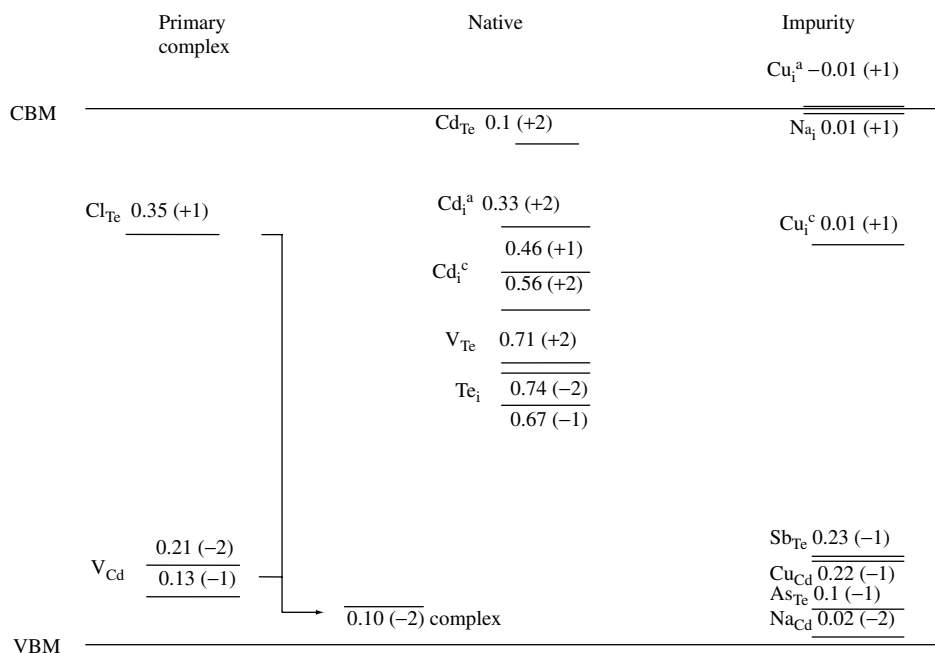


Figure 14.5 CdTe band structure with doping and defect levels. Charge states are in parentheses; energy is in electron volts measured from the conduction band for donor (positive) states and valence band for acceptor (negative) states. The superscripts a and c represent alternative interstitial sites. (Adapted from Wei S, Mtg. Record, National CdTe R&D Team Meeting (2001) Appendix 9 [60])

effects; (2) discovering the effect of grain boundaries on film properties and junction behavior; and (3) controlling film properties over very large area, encompassing $\sim 10^{12}$ grains per square meter for a CdTe module having 1- μm -wide grains. For CdTe/CdS solar cell development, these challenges have been met through advancing characterization techniques and empirical optimization of film deposition and postdeposition treatments.

A detailed review of the analytical techniques employed to probe the microstructure, microchemistry, and electronic properties of thin-film CdTe/CdS solar cells is beyond the scope of this chapter. However, several powerful methods have emerged to provide a quantitative assessment of film properties and are discussed elsewhere generally [63, 64], and specifically in terms of CdTe/CdS solar cells [65–67]. Some of these methods may ultimately find application as diagnostic sensors for in-line process-control feedback during module manufacture. These are listed below, accompanied by one or more references in which the techniques are applied to CdTe/CdS thin-film solar cells.

Morphology and structure:

- Scanning Electron Microscopy (SEM) [68]
- Transmission Electron Microscopy (TEM) [69]
- Atomic Force Microscopy (AFM) [70]
- X-Ray Diffraction (XRD) [71]

Bulk chemical composition:

- Energy Dispersive X-ray Spectroscopy (EDS) [72]
- X-Ray Diffraction (XRD) [73]
- Auger Electron Spectroscopy (AES) [74]
- Secondary Ion Mass Spectroscopy (SIMS) [75, 76]

Surface chemical composition:

- X-ray Photoemission Spectroscopy (XPS) [77]
- Glancing Incidence X-Ray Diffraction (GIXRD) [78]

Optoelectronic properties:

- Optical absorption [79]
- Ellipsometry [80]
- Raman [81]
- Photoluminescence (PL) [82, 83]

Junction analysis:

- Current–voltage versus illumination and temperature ($J-V-T$) [28, 84]
- Spectral response [23]
- Capacitance–voltage ($C-V$) [85]
- Optical Beam Induced Current (OBIC) [86]
- Electron Beam Induced Current (EBIC) [87]
- Cathode Luminescence (CL) [88]

Numerous methods have been employed to deposit CdTe thin films for solar cells, as detailed in the special issue of the *International Journal of Solar Energy* [89] and other review articles [90–92]. We will review eight methods that have demonstrated viability for the commercial manufacture of CdTe solar cells and modules over the past decade. Figure 14.6 presents schematic views of each fabrication procedure, including nominal temperature and pressure conditions, film thickness, and growth rate. The

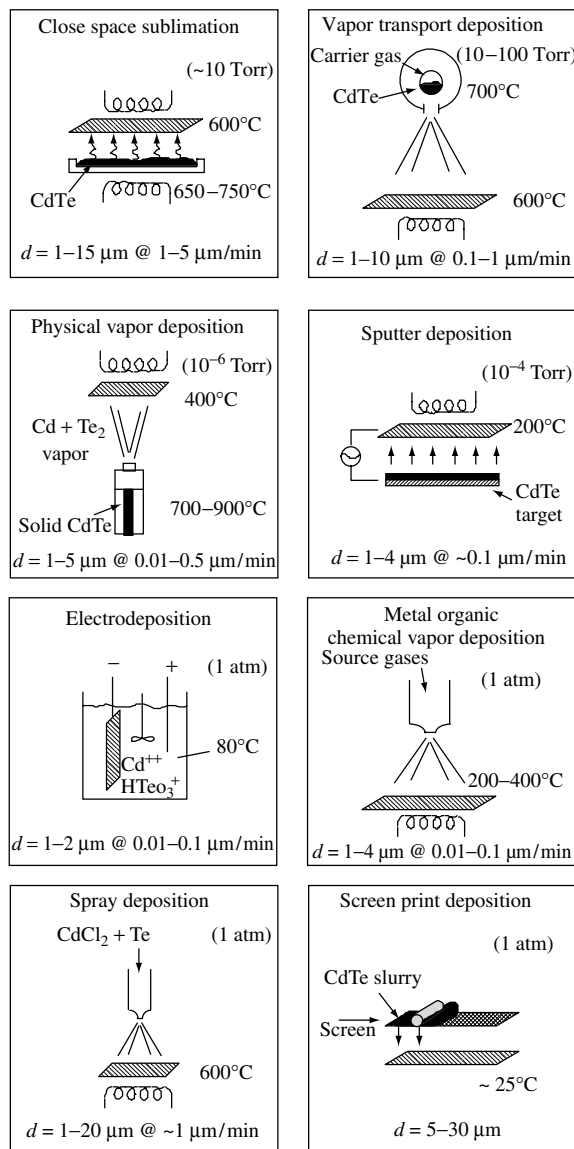


Figure 14.6 Schematic representations of eight CdTe thin-film deposition techniques. The substrate in each view is the cross-lined rectangle. Film thickness, d , and growth rate are shown at the bottom of each panel

presentation is organized by three chemical concepts: (1) condensation/reaction of Cd and Te₂ vapors on a surface (PVD, VTD, CSS, and sputter deposition), (2) galvanic reduction of Cd and Te ions at a surface (electrodeposition), (3) reaction of precursors at a surface [metal-organic chemical vapor deposition (MOCVD), screen-print deposition, and spray deposition].

14.2.1 Condensation/Reaction of Cd and Te₂ Vapors on a Surface

14.2.1.1 Physical vapor deposition (PVD)

The basis for vapor deposition of CdTe is the equilibrium between Cd and Te₂ vapors and CdTe solid, $\text{Cd} + 1/2\text{Te}_2 \rightleftharpoons \text{CdTe}$. As a consequence, CdTe can be deposited by coevaporation from elemental sources, by direct sublimation from a CdTe source or by vapor transport using a carrier gas to entrain and deliver Cd and Te₂ vapors from either elemental or CdTe sources. Congruent sublimation of the CdTe compound fixes the gas-phase composition for deposition from a CdTe source, and the relatively low vapor pressure of CdTe compared to elemental Cd and Te facilitates the deposition of single-phase solid films over a wide range of substrate temperatures (refer to Figure 14.3(b)). Similar considerations allow coevaporation from multiple II-VI binary sources to deposit alloys in pseudobinary systems such as $\text{CdZn}_{1-x}\text{Te}_x$ and $\text{CdTe}_{1-x}\text{S}_x$.

Evaporation can be carried out from open crucibles or from Knudsen-type effusion cells, with the latter providing superior control over beam distribution and utilization. For effusion-cell evaporation, the deposition rate and uniformity of the species arriving at the substrate are controlled by source temperature, effusion-cell geometry, source to substrate distance, and total pressure [93, 94]. Within the effusion cell, mass transport to the nozzle exit occurs in a transitional flow regime, between free molecular flow and diffusion-limited flow. Effusion cells are typically constructed of boron nitride or graphite and are radiatively heated. For deposition in moderate vacuum, $\sim 10^{-6}$ Torr, with a CdTe source effusion cell with 0.5-cm-diameter orifice and a temperature of 800°C, at a source to substrate distance of 20 cm, a deposition rate of ~ 1 $\mu\text{m}/\text{min}$ is obtained on a substrate at a sufficiently low temperature ($\sim 100^\circ\text{C}$) for Cd and Te sticking coefficients to approach unity. At higher substrate temperatures, the sticking coefficients of impinging Cd and Te decrease, resulting in a lower deposition rate, imposing a practical limit to substrate temperature of less than 400°C for modest CdTe utilization. As-deposited films exhibit (111) preferred orientation and normal grain-size distribution with a mean grain diameter that depends on film thickness and substrate temperature; for 2- μm -thick films, the mean grain diameter ranges from ~ 100 nm at 100°C to ~ 1 μm at 350°C. The physical vapor deposition (PVD) process has been investigated by university (Stanford University [95], Institute of Energy Conversion at University of Delaware [96]) and industrial (Canrom and Central Research Laboratory at Japan Energy Corporation [97]) groups.

14.2.1.2 Close-space sublimation (CSS)

To evaporate CdTe films onto substrates at temperatures above 400°C, reevaporation of Cd and Te from the growing CdTe surface limits the deposition rate and utilization. This can be mitigated by depositing at higher total pressure, ~ 1 Torr, but mass transfer from the source to the substrate becomes diffusion-limited, so the source and substrate must be brought into close proximity. For close-space sublimation (CSS), the CdTe source material is supported in a holder having the same area as the substrate; the source holder and substrate cover serve as susceptors for radiative heating and conduct heat to the CdTe source and the substrate, respectively. An insulating spacer allows thermal isolation of the source from the substrate, so that a temperature differential can be sustained throughout the duration of the deposition. The ambient for deposition typically contains a nonreactive

gas such as N₂, Ar, or He. A small partial pressure of O₂ appears to be crucial for obtaining good film density and solar cell junction quality. As-deposited CSS films deposited above 550°C exhibit nearly random orientation and normal grain size distribution with mean grain size that is comparable to film thickness. The CSS process has been intensively investigated by groups at Kodak [98], USF [99, 100], NREL [101], Matsushita [102], and Antec [103, 104] and has yielded the highest small-area cell performance of any process shown in Figure 14.6. Commercial development is presently under way at Antec, GmbH.

14.2.1.3 Vapor transport deposition (VTD)

VTD allows high-rate deposition at high substrate temperature at pressures approaching 0.1 atm onto moving substrates. While CSS is diffusion-limited, VTD works by convective transfer of a vapor stream saturated with Cd and Te to the substrate, where supersaturation of the Cd and Te vapors results in condensation and reaction to form CdTe. The CdTe source consists of a heated chamber containing solid CdTe in which the carrier gas mixes with the Cd and Te vapors and is exhausted through a slit over or under the moving substrate at a distance on the order of ~1 cm. The geometrical configuration of the source influences the uniformity and utilization of the vapors in the carrier gas. The carrier-gas composition can be varied, as with CSS, to include N₂, Ar, He, and O₂. As-deposited VTD films are similar to CSS films, with nearly random orientation and normal grain size distribution with mean grain size that is comparable to film thickness [105]. The VTD process can provide a very high deposition rate onto moving substrates and is currently being investigated by the Institute of Energy Conversion and is under development by First Solar, LLC [106].

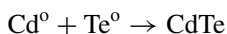
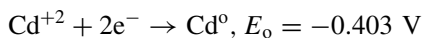
14.2.1.4 Sputter deposition

CdTe films have been deposited by radio-frequency magnetron sputtering from compound targets. Mass transfer of Cd and Te occurs via ablation of the CdTe target by Ar⁺, followed by diffusion to the substrate and condensation. Typically, deposition is carried out at a substrate temperature less than 300°C and at pressures ~10 mTorr. As-deposited films 2-μm-thick deposited at 200°C exhibit mean grain diameter ~300 nm and nearly random orientation. The sputter-deposition technique has been investigated by groups at the University of Toledo [107] and NREL [108].

14.2.2 Galvanic Reduction of Cd and Te Ions at a Surface

14.2.2.1 Electrodeposition

Electrodeposition of CdTe consists of the galvanic reduction of Cd and Te from Cd²⁺ and HTeO₂⁺ ions in acidic aqueous electrolyte. The reduction of these ions utilizes six electrons in the following reactions:



The large difference in reduction potential necessitates limiting the concentration of the more positive species, Te, to maintain stoichiometry in the deposit. In practice, the low Te species concentration (10^{-4} M) limits the CdTe growth rate due to Te depletion in the solution at the growing surface and subsequent mass transport. To overcome this, the electrolyte is vigorously stirred, and different methods of Te replenishment are employed. Thickness and deposition area are limited by the ability to maintain deposition potential over the entire surface of the growing film. As-deposited films can be fabricated as stoichiometric CdTe, Te-rich (by increasing Te species concentration in the bath) or Cd-rich (by depositing at low potentials with limited Te species concentration). As-deposited electrodeposited CdTe films on CdS thin-film substrates exhibit strong (111) orientation with columnar grains having a mean lateral diameter of 100 to 200 nm. The basis for this technology has been formalized in the open literature [109]. Electrodeposition of CdTe has been intensively studied by the group at Monosolar [110], Ametek [111], and the University of Texas [112]. In the 1980s, the Monosolar process was transferred to SOHIO and thence to BP Solar, where commercial development took place at the factory in Fairfield, California. In the early 1990s, the Ametek process was transferred to the Colorado School of Mines in Golden Colorado.

14.2.3 Precursor Reaction at a Surface

14.2.3.1 *Metal organic chemical vapor deposition (MOCVD)*

MOCVD is a nonvacuum technique for depositing CdTe films at moderately low temperature from organic Cd and Te precursors such as dimethylcadmium and diisopropyltellurium in hydrogen carrier gas. The substrates are supported on graphite susceptors and can be heated radiatively or by coupling to a radio frequency generator. Deposition occurs by pyrolytic decomposition of the source gases and reaction of the Cd and Te species. As a consequence, the growth rate depends strongly on the substrate temperature, which typically ranges from 200 to 400°C. As-deposited films 2- μ m-thick deposited at 400°C exhibit columnar grain structure with lateral grain diameter ~ 1 μ m. The MOCVD process has been investigated by groups at SMU/USF [113] and Georgia Institute of Technology [114].

14.2.3.2 *Spray deposition*

Spray deposition is a nonvacuum technique for depositing CdTe from a slurry containing CdTe, CdCl₂, and a carrier such as propylene glycol. The slurry can be sprayed onto unheated or heated substrates, after which a reaction/recrystallization treatment is performed. The application of spray deposition to CdTe films was developed by John Jordan (Photon Energy Corporation) during the 1980s. The company was sold to Coors in 1995 and had its name changed to Golden Photon. Cells with >14% efficiency were fabricated, but commercial development ceased in 1997. In this process, the mixture was sprayed onto the substrates at room temperature and baked at 200°C, followed by a bake in the presence of O₂ at 350 to 550°C, a mechanical densification step, and a final treatment at 550°C. Films produced by this method vary in morphology, grain size, and porosity, but films used to make high-efficiency cells exhibited a 1- to 2- μ m-thick dense region near the CdTe–CdS interface, a relatively porous back surface region, and random crystallographic

orientation. A dramatic consequence of the fabrication process was the consumption of the CdS layer, leading to a nearly uniform $\text{CdTe}_{1-x}\text{S}_x$ alloy throughout the film thickness, which reduced the absorber-layer band gap to ~ 1.4 eV. In the highest-efficiency cells made by spray deposition, CdS diffusion and subsequent alloy formation consumed most of the CdS film, resulting in an enhanced blue-spectral response and correspondingly high short-circuit densities. The method was extensively investigated by the group at Golden Photon [115, 116].

14.2.3.3 Screen-print deposition

Screen-print deposition is perhaps the simplest of the CdTe techniques, combining Cd, Te, CdCl_2 , and a suitable binder into a paste that is applied to the substrate through a screen. Following a drying step to remove binder solvents, the layer is baked at temperatures up to 700°C to recrystallize the film and activate the junction. Films fabricated by this method typically have a thickness ranging from 10 to 20 μm with lateral grain dimension of ~ 5 μm and random orientation. Screen-printed CdTe can be traced back to the 1970s with the pioneering work of Matsushita [117] and subsequently by groups at the University of Seoul [118] and the University of Ghent [119].

14.3 CdTe THIN-FILM SOLAR CELLS

All high-efficiency CdTe solar cells to date have essentially the same *superstrate* structure as that successfully demonstrated by Bonnet and Rabenhorst in 1972 [26]. This structure is depicted in Figure 14.7. The alternative *substrate* configuration, with the TCO/CdS/CdTe deposited onto an opaque substrate, has been much less successful, primarily because of poor CdS/CdTe junction quality and poor ohmic CdTe contact, resulting from chemical instability of the back contacts and from copper diffusion out of the back contact toward the CdTe surface during film growth.

The primary photodiode junction occurs between the *p*-type CdTe absorber and the *n*-CdS window layer. There are, however, a number of complicating factors, such as the need for a high-resistance oxide layer when the CdS is thin, the need for a thermal treatment with CdCl_2 and oxygen to improve the CdTe quality, the interdiffusion of CdS and CdTe, and the barrier associated with the back contact. The following sections will address these complications.

14.3.1 Window Layers

The first step in the fabrication of a superstrate CdTe cell is to coat the glass with a transparent conducting oxide (TCO), such as SnO_2 , indium–tin oxide, $\text{In}_2\text{O}_3\text{:Sn}$, referred to as ITO, or cadmium stannate, Cd_2SnO_4 , which serves as the front contact. To obtain high current density in the completed cell, the CdS layer needs to be very thin, which, owing to its polycrystallinity, raises the possibility of local shunting or excessive forward current. It has been found that the deposition of a second, highly resistive, transparent oxide layer, referred to as the HRT layer, between the TCO and CdS significantly ameliorates this problem and improves junction quality and uniformity in a manner analogous to

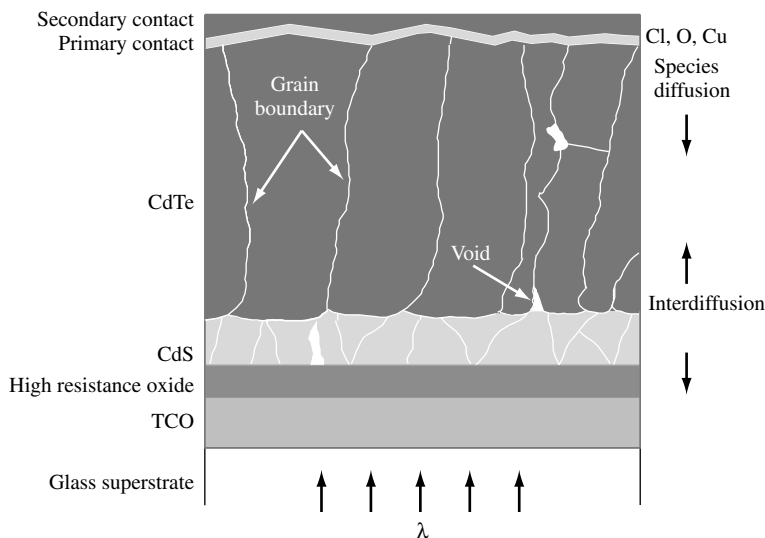


Figure 14.7 Basic CdTe solar cell structure. The polycrystalline nature of the CdS and CdTe layers are indicated schematically and are not to scale

that found for CuInSe₂/CdS and a-Si thin-film cells [120]. Materials used for the resistive layer include SnO₂ [121], In₂O₃ [122, 123], Ga₂O₃ [105], and Zn₂SnO₄ [124].

Most CdTe cells utilize *n*-type CdS for the window layer immediately adjacent to the CdTe. The processing possibilities for depositing good-quality CdS are nearly as varied as those shown in Figure 14.6 for CdTe and include chemical bath deposition, sputter deposition, and physical vapor deposition. The choice is usually driven by compatibility with the other deposition processes in a fabrication line. It is generally desirable to keep the CdS layer as thin as possible to allow a high fraction of the photons with energy above its band gap to reach the CdTe absorber and hence produce a high photocurrent.

In practice, as will be discussed in more detail later, cell-processing conditions often promote interdiffusion between CdTe and CdS. The resulting band gap shift in CdS reduces the window-layer transmission and lowers the short-wavelength quantum efficiency [125, 126]. This effect can be minimized either by heat treatment of the CdS with CdCl₂ to recrystallize the film or by judicious control of device processing to reduce the remaining CdS thickness [124] effectively to zero [116]. Thin-film CdTe cells with the CdS layer omitted altogether, however, have not performed well as of this writing (see, for example, Table 2 in Reference [122]).

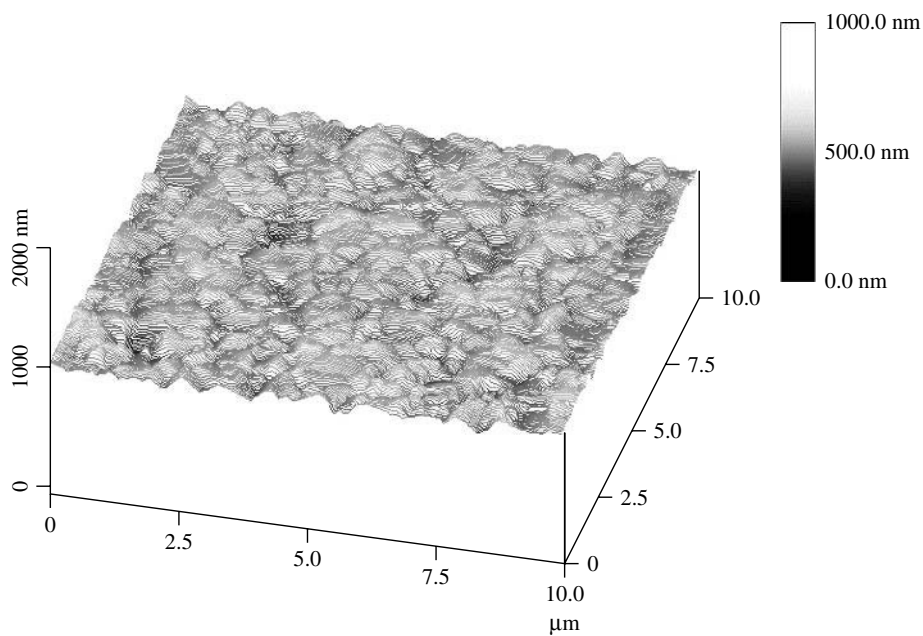
Another strategy to reduce window absorption has been to mix CdS with ZnS to increase the band gap of the layer, and hence the photon transmission, but simple mixing has not produced net performance gains. The highest-efficiency CdTe cells to date have used Cd₂SnO₄ TCO and Zn₂SnO₄ HRT bilayer superstrates to take advantage of their wide optical band gaps and inherent conductive properties, with the Cd₂SnO₄ serving as the TCO layer and Zn₂SnO₄ as the HRT layer. An additional feature of this strategy is that the Zn₂SnO₄ HRT layer contributes to CdS consumption during processing [127].

14.3.2 CdTe Absorber Layer and CdCl₂ Treatment

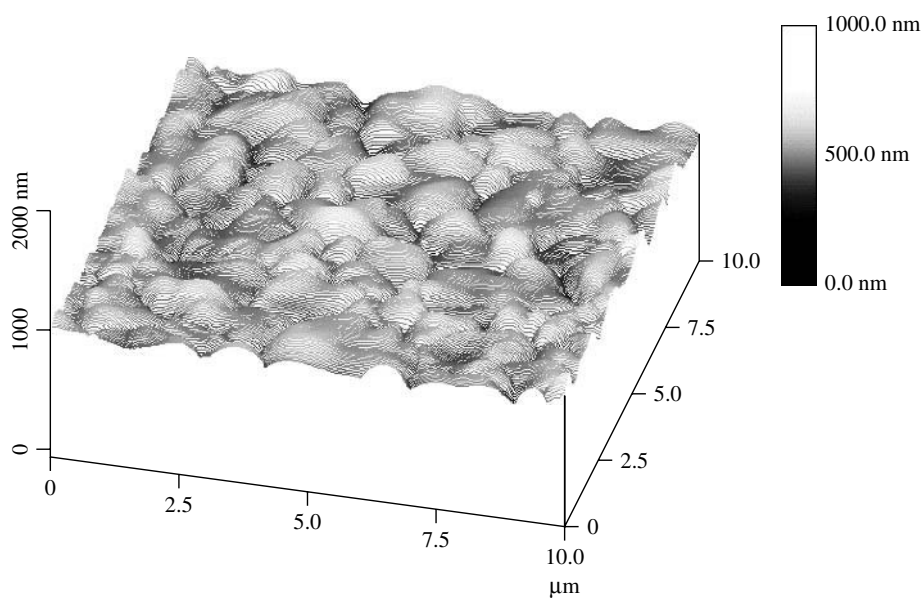
The large number of successful techniques for deposition of device-quality CdTe films was shown schematically in Figure 14.6. However, in cases of chloride-free deposition techniques such as physical vapor deposition (PVD), the actual deposition of the CdTe film has been found to be less critical than the postdeposition processing, which generally involves exposure to a high-temperature processing step followed by exposure to a chlorine-containing species and oxygen at $\sim 400^\circ\text{C}$, referred to as the “CdCl₂ treatment.” The treatment step has been performed in a variety of ways, such as dipping the CdTe layer in a CdCl₂:CH₃OH or CdCl₂:H₂O solution followed by drying to precipitate a CdCl₂ film [128, 129] by treatment in CdCl₂ vapor [130, 131] or by exposure to HCl [132] or Cl₂ gas [133]. Chlorine species may also be incorporated during CdTe film formation, in the form of Cl[−] ions in an electrodeposition bath [134] or as a component of a screen-printing slurry [68]. The typical temperature–time range for the thermal cycle following chlorine incorporation is from 380 to 450°C for 15 to 30 min, depending on CdTe film thickness, with thicker films requiring longer treatment time.

The changes induced by chlorine incorporation and subsequent heat treatment depend on the prior thermochemical history of the CdTe/CdS structure. For example, the treatment can promote recrystallization and grain growth in films having submicrometer initial CdTe crystallite size [135]. The change in morphology and structure is shown in Figures 14.8 and 14.9. Figure 14.8 shows atomic force micrographs of the surface morphology of PVD CdTe, deposited at 250°C, before and after treatment at 420°C in CdCl₂ and air vapor. Figure 14.9 shows cross-sectional TEM images of changes in grain size and crystallographic defects in the junction region of a CdTe/CdS/ITO structure deposited by PVD onto a smooth Si wafer. Depositing the structure on a Si wafer facilitated the mechanical preparation of the sample for cross-sectional thinning. Table 14.2 more generally compares the changes in grain size, aspect ratio, and crystallite orientation for CdTe deposited by several different methods. For CdTe films having submicrometer initial crystallite size, such as shown in Figure 14.8, significant recrystallization occurs during the CdCl₂ treatment. This takes two forms: (1) intragrain, or primary, recrystallization changes grain orientation from typically (111) to random (see Figure 14.10) and (2) intergrain, or secondary, recrystallization results in grain coalescence. The phrase “fluxing agent” has been coined in reference to the role of CdCl₂ in promoting grain growth, although the secondary recrystallization does not always occur, depending on the thermochemical history of the film and the initial grain size. For films deposited at high temperature, having large initial grain size, annealed prior to CdCl₂ exposure, or containing the native oxide, CdTeO₃, little measurable grain growth (secondary recrystallization) occurs during CdCl₂ treatment. This is because surface energy is already minimized or is pinned by the presence of the oxide. Under these processing conditions, film randomization is the predominant effect, showing that CdCl₂ still exerts an intragrain influence on lattice arrangement.

The postdeposition treatment also modifies the electronic properties. Air-heat treatment alone, at temperatures above $\sim 500^\circ\text{C}$, can reduce the CdTe sheet resistance up to three orders of magnitude [136]. Treatment with CdCl₂ in air likewise reduces resistivity, by the combination of recrystallization and creation of acceptor states. The primary electronic effect of Cl incorporation seems to be the formation of an acceptor complex with Cd vacancies (see Figure 14.5). Both the single-donor and the double-acceptor states are



(a)



(b)

Figure 14.8 AFM images comparing PVD CdTe/CdS thin-film structures (a) before and (b) after heat treatment in CdCl_2 vapor at 420°C for 20 min

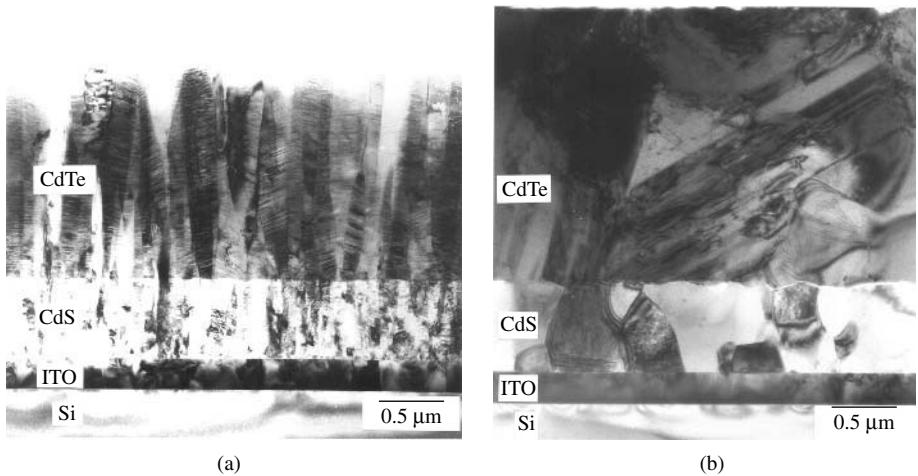


Figure 14.9 TEM images comparing PVD CdTe/CdS thin-film structures (a) before and (b) after CdCl_2 heat treatment at 420°C for 20 min. Average grain size increased from roughly 0.1 to $0.5\ \mu\text{m}$ in both CdTe and CdS

Table 14.2 Structural changes of CdCl_2 HT on CdTe deposited by different methods. Data from films examined by B. E. McCandless. For sprayed and screen-printed cells, random film orientation is obtained as a result of the film formation process

Deposition method	Film thickness [μm]	Mean grain size: D Init \rightarrow CdCl_2 HT [μm]	Orientation Init \rightarrow CdCl_2 HT
PVD	4	$0.1 \rightarrow 1$	$(111) \rightarrow (220)$
ED	2	$0.1 \rightarrow 0.3$	$(111) \rightarrow (110)$
Spray	10	$10 \rightarrow 10$	Rand
Screen	12	~ 10	Rand
VTD	4	$4 \rightarrow 4$	Rand \rightarrow Rand
CSS	8	$8 \rightarrow 8$	Rand \rightarrow Rand
Sputter	2	$0.3 \rightarrow 0.5$	$(111) \rightarrow (?)$
MOCVD	2	$0.2 \rightarrow 1$	$(111) \rightarrow$ Rand

pushed closer to the band edges, resulting in a single, relatively shallow acceptor state. Although this complex is a more effective dopant than the Cd vacancies alone, excess Cl can lead to compensating Cl_{Te} donors.

The impact of CdCl_2 treatment on cell operation is increased photocurrent and open-circuit voltage, and reduced shunting. Figure 14.11 compares the light $J-V$ behavior of three PVD cells having $4\text{-}\mu\text{m}$ -thick CdTe and $0.2\text{-}\mu\text{m}$ -thick CdS, processed with the same back contact but with no postdeposition treatment, air-heat treatment at 550°C , and optimized CdCl_2 treatment at 420°C for 20 min in air. With no treatment, the device exhibits very low photocurrent and high series resistance. The spectral response is low

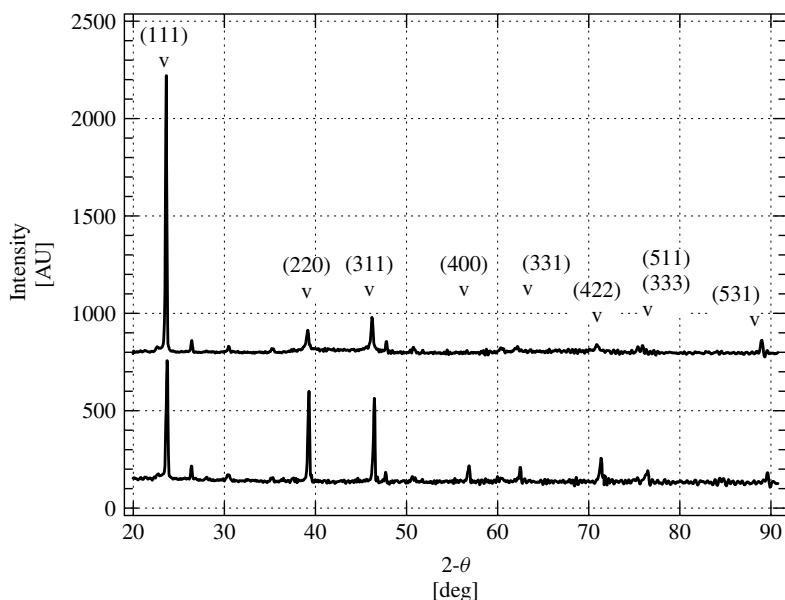


Figure 14.10 X-ray diffraction patterns of PVD CdTe/CdS thin-film structures before and after vapor CdCl₂ heat treatment at 420°C for 20 min, showing randomization of the film orientation. The primary peaks are due to the 1.5-μm-thick CdTe layer; the other peaks are due to the underlying CdS and ITO films

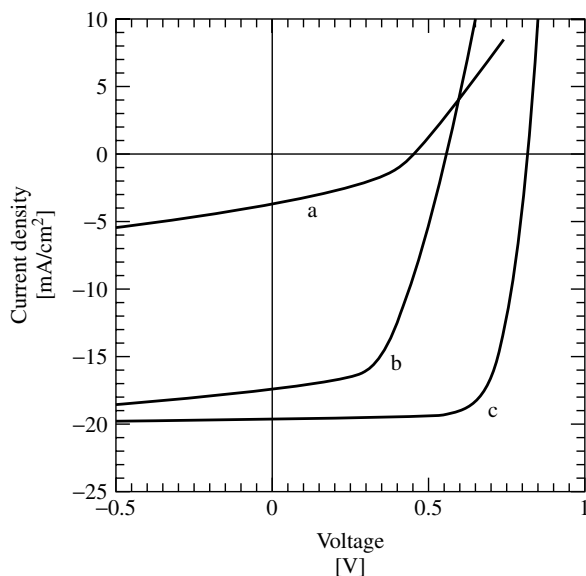


Figure 14.11 Light AM1.5 $J-V$ curves of PVD devices with Cu₂Te/C contacts and different post-deposition processing: (a) no heat treatment; (b) treatment at 550°C for 5 min in air; (c) treatment in CdCl₂ vapor at 420°C for 20 min in air [105]

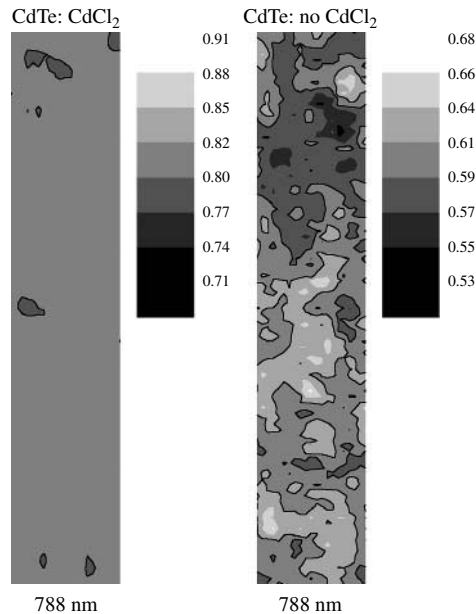


Figure 14.12 Local variations in quantum efficiency with 1- μm beam and $\lambda = 788\text{ nm}$. Areas shown are $50 \times 10\text{ }\mu\text{m}$

overall and exhibits a peak near the CdTe band edge, suggesting *p-i-n* device operation [137]. With either air treatment or vapor CdCl_2 + air treatment, the $J-V$ and spectral response behavior correspond to *p-n* device operation, with optimal properties obtained for the vapor CdCl_2 + air treatment. For devices made by other methods, similar behavior is obtained, but the starting condition (Figure 14.11a) can be improved by deposition at high temperature in an oxygen-containing ambient.

The effect of the CdCl_2 treatment on photocurrent microuniformity is shown in Figure 14.12, for cells with CdTe deposited by CSS. The QE map on the left was made on a cell following a typical CdCl_2 treatment, and shows spatially uniform collection. The map on the right was for a cell fabricated without the CdCl_2 treatment and exhibits considerable nonuniformity [138]. The light intensity for these maps is nearly 100 mW/cm^2 and the light spot is slightly smaller than $1\text{ }\mu\text{m}$. The large local reductions in photocurrent without CdCl_2 treatment are areas of high resistance associated with grain boundaries. With the use of the CdCl_2 treatment, spatial-junction uniformity is improved by the electronic incorporation of Cl and O species and alloy formation by diffusion of CdS into CdTe. The QE of the sample with CdCl_2 treatment is ~ 0.82 over 95% of the measured area, while that of the sample without CdCl_2 treatment ranges from 0.50 to 0.68.

14.3.3 CdS/CdTe Intermixing

All CdS/CdTe cells are exposed to processing temperatures of at least 350°C during CdCl_2 treatment. In some cases, such as spray pyrolysis, much higher temperatures are involved. Hence, a chemical reaction between CdTe and CdS can occur and this is the

driving force for bulk and grain-boundary interdiffusion of CdTe and CdS. It has been widely reported that a continuous CdTe–CdS solid-solution alloy series can be formed by codeposition of CdTe and CdS at temperatures less than 200°C. The optical band gap of these alloys varies with the composition according to $E_g(x) = 2.40x + 1.51(1 - x) - bx(1 - x)$, with bowing parameter, $b \sim 1.8$, as shown in Figure 14.13 [139]. However, thermal treatment of alloy films above 400°C can induce phase segregation, with the miscibility gap found for equilibrated CdTe–CdS mixed crystals.

Numerous references have established the T – x phase relations in CdTe–CdS mixed crystals at temperatures above 625°C, which exceeds the temperatures typically used to deposit and process thin-film CdTe/CdS structures. This has been extended down to 360°C by lattice-parameter determination of equilibrated CdTe_{1–x}S_x alloy films, as shown in Figure 14.14 [146]. Thermodynamic analysis of the asymmetric phase boundaries using nonideal solution thermodynamics reveals positive values of excess-mixing enthalpies $\Delta H^{\text{EX}} = 3.5$ kcal/mol for CdS into CdTe and $\Delta H^{\text{EX}} = 5.6$ kcal/mol for CdTe into CdS. For CdS dissolved in CdTe, the experimentally obtained excess-mixing enthalpy supports those calculated from first principles band structure theory for the CdTe–CdS system [147].

The crystallographic forms of the solid alloys are the zincblende (F-43 m) structure for CdTe_{1–x}S_x and the wurtzite (P6₃mc) structure for CdS_{1–y}Te_y. The zincblende transition to the wurtzite structure in metastable films occurs at $x = 0.3$, and the lattice parameter within each structure type follows Vegard's rule. Metastable and equilibrated CdTe_{1–x}S_x alloy films exhibit the same dependence of E_g , with minimum at 1.39 eV, corresponding to the zincblende–wurtzite transition.

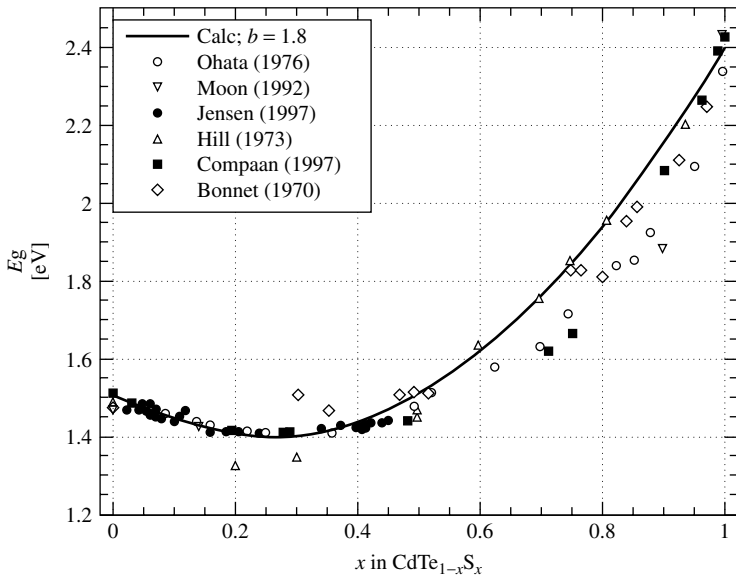


Figure 14.13 Optical band gap of CdTe_{1–x}S_x alloy thin films versus composition. (Data listed in order from References [140–145])

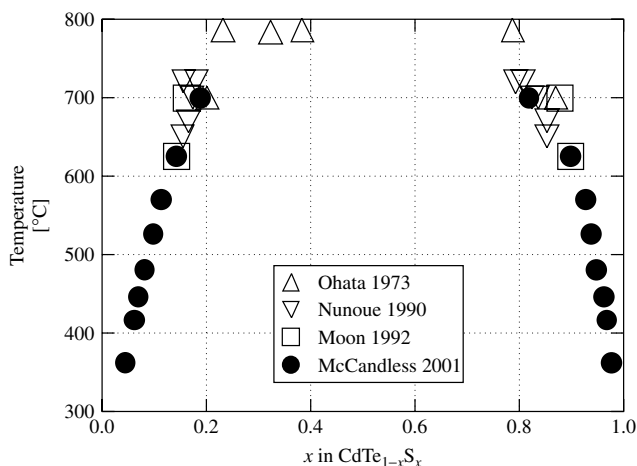


Figure 14.14 CdTe–CdS pseudobinary phase diagram. (Data listed in order from References [73, 140, 145, 148])

The formation of $\text{CdTe}_{1-x}\text{S}_x$ and $\text{CdS}_{1-y}\text{Te}_y$ alloys in the absorber layer occurs by interdiffusion between CdS and CdTe during CdCl_2 treatment in air [135, 204]. Diffusion of CdTe into CdS can reduce the transmissive properties of the window from 500 to 650 nm, but is mitigated by heat treatment of the CdS layer prior to CdTe deposition to increase CdS grain size and density. However, diffusion of CdS into CdTe is a faster process and is more difficult to control, especially for cell structures with ultrathin, <100 nm, CdS films. The progressive diffusion, which creates a distribution of lattice parameters within the film, can be easily detected with X-ray diffraction line-profile analysis (Figure 14.15).

Quantifying the diffusion process for films of a known grain structure showed that the diffusion proceeds via Fickian bulk and grain-boundary diffusion processes having Arrhenius temperature dependence [149] (Figure 14.16). Similar bulk diffusivities were found for CdS/CdTe couples using single-crystal CdTe and thin-film couples in *substrate* and *superstrate* configurations, yielding an activation energy of ~ 3.0 eV, corresponding to Cd self diffusion via Cd interstitials. Likewise, similar grain-boundary diffusivities were obtained for *substrate* and *superstrate* thin-film couples, with an activation energy of ~ 2.0 eV (Figure 14.17). The bulk diffusivity was weakly sensitive to the chemical composition of the treatment ambient, as shown in Figure 14.18. However, the grain-boundary diffusion process is enhanced by the partial pressures of CdCl_2 and O_2 during the CdCl_2 treatment. Finally, it has been demonstrated that grain-boundary diffusion can be retarded by oxidizing grain boundaries prior to exposure to CdCl_2 species [122] or by deposition of CdTe films in an oxygen-containing ambient.

Thus, alloy formation can be more pronounced in films deposited at low temperature having small grains and high grain-boundary density, such as by electrodeposition. In such films, a high partial pressure or concentration of CdCl_2 together with O_2 during CdCl_2 treatment will result in considerable alloy formation. In addition, alloy formation is dramatically enhanced for cells with CdTe deposited at high temperature in the presence of Cl species during growth, such as spray pyrolysis.

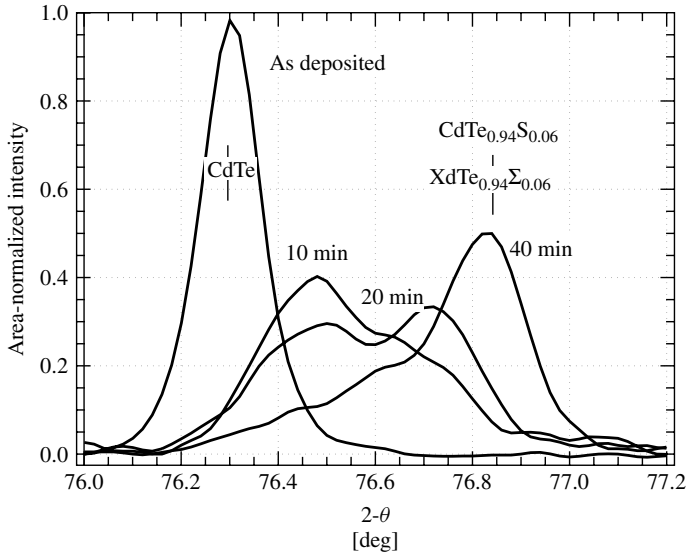


Figure 14.15 Time-progressive X-ray diffraction line profiles for the (511)/(333) reflection for PVD CdTe/CdS thin-film structures deposited at 250°C and treated in CdCl₂:Ar:O₂ vapor at 420°C. Positions of pure CdTe and CdTe_{1-x}S_x alloy with $x = 0.06$ are indicated

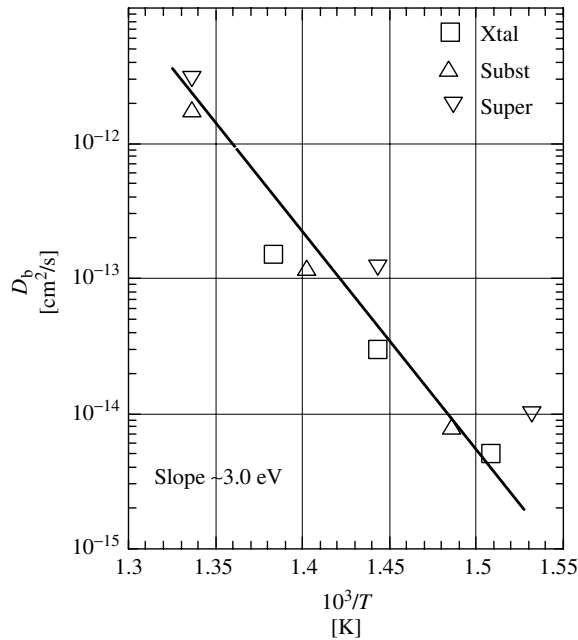


Figure 14.16 Arrhenius plot of bulk-diffusion coefficients versus inverse of treatment temperature for values obtained by modeling XRD line profiles of thin-film CdTe/CdS samples and from AES depth profiling of S distribution in CdTe single crystal [73]

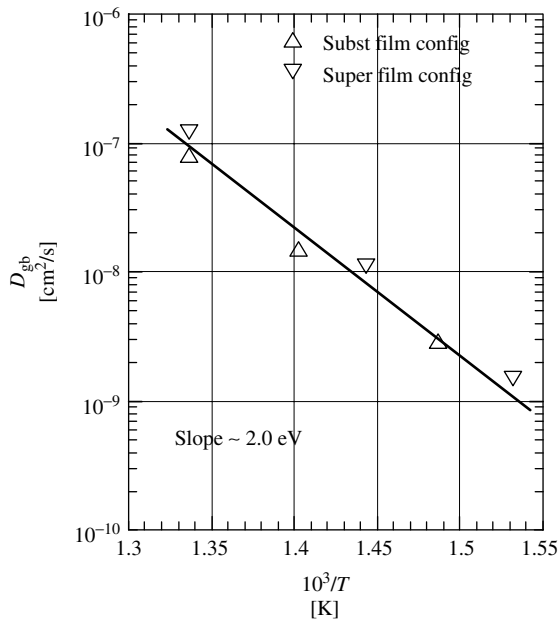


Figure 14.17 Arrhenius plot of grain-boundary diffusion coefficients versus inverse of treatment temperature for values obtained by modeling XRD line profiles of thin-film CdTe/CdS samples [73]

In cells, alloy formation has both beneficial and detrimental effects. The interdiffusion process narrows the absorber-layer band gap, resulting in higher long-wavelength quantum efficiency. Although this gain is somewhat offset by a reduction in the built-in voltage, open-circuit voltages exceeding 820 mV have been obtained in cells having alloyed $\text{CdTe}_{1-x}\text{S}_x$ absorber layers with composition $x > 0.05$, made by spray pyrolysis [150]. Intermixing reduces interfacial strain [68] and may reduce the dark recombination current [78]. The CdS film thickness is reduced, which can be beneficial for window transmission, but nonuniform CdS consumption can result in lateral junction discontinuities. The $\text{CdTe}_{1-x}\text{S}_x$ alloy formation is detected in XRD line profiles of the absorber layer and in the long-wavelength spectral response. This correlation between compositionally broadened XRD line profiles and the long-wavelength QE edge is illustrated in Figure 14.19 for XRD and QE measurements of completed cells. For CSS cells, deposited at high temperature and having large grains, the absorber layer exhibits a narrow (511)/(333) XRD profile at the CdTe position, indicating a negligible degree of alloy formation, and hence low CdS diffusion into CSS-deposited CdTe. This is seen in the QE plot, where the long-wavelength edge occurs at the wavelength expected for CdTe. In contrast, the cell made by spray pyrolysis, with the CdTe film formed at high temperature in the presence of CdCl_2 , exhibits an asymmetrical XRD line profile with its peak near the one expected for the $\text{CdTe}_{0.96}\text{S}_{0.05}$ and a tail extending toward pure CdTe. The XRD line profile thus indicates nonuniform S distribution in the absorber layer, evident in the QE plot as a shallow drop in the long-wavelength response. The PVD case is intermediate to the CSS and spray cases, having smaller grains than CSS films and receiving less exposure to CdCl_2 than sprayed films. Thus, it appears that apart

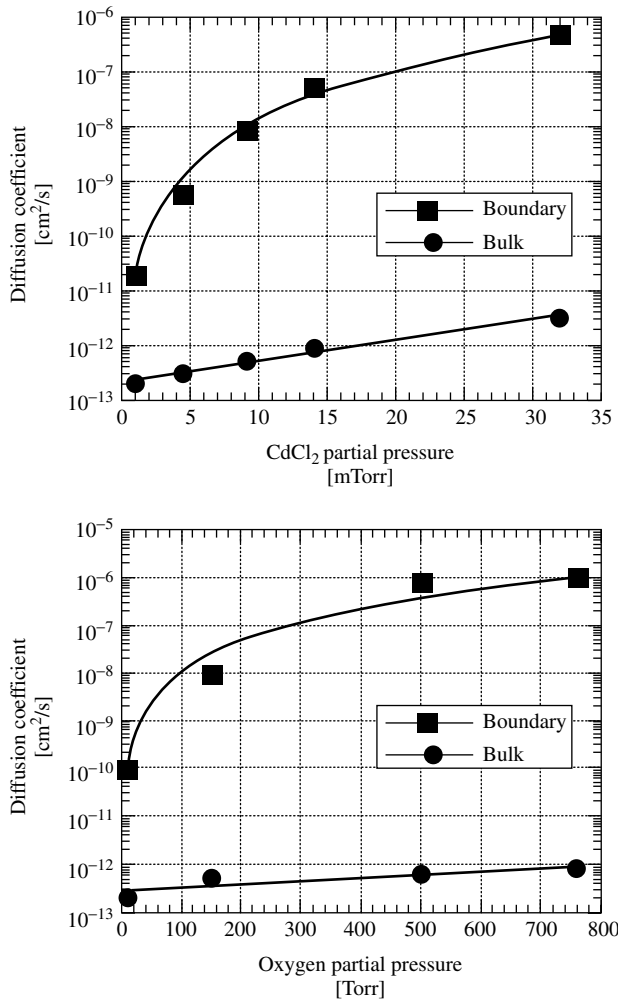


Figure 14.18 Sensitivity of bulk and grain-boundary diffusion coefficients (a) to p_{CdCl_2} at constant $p_{\text{O}_2} \sim 125$ Torr, at $T = 420^\circ\text{C}$, and (b) to p_{O_2} at constant $p_{\text{CdCl}_2} = 9$ mTorr, at $T = 420^\circ\text{C}$

from the differences in current generation, device operation is fundamentally similar for cells with differing amounts of $\text{CdTe}_{1-x}\text{S}_x$ alloy in the absorber layer.

14.3.4 Back Contact

The top region shown in Figure 14.7 is the back contact, consisting of a primary contact to CdTe, which typically consists of a tellurium-containing p^+ surface, and a secondary contact, which is the current-carrying conductor. As with other p -type semiconductors, there is a tendency to form a Schottky barrier with many metals, and achieving a low-resistance ohmic contact has proven to be challenging. The most common strategy is to form a Te-rich surface by selective chemical etching and then apply copper or a

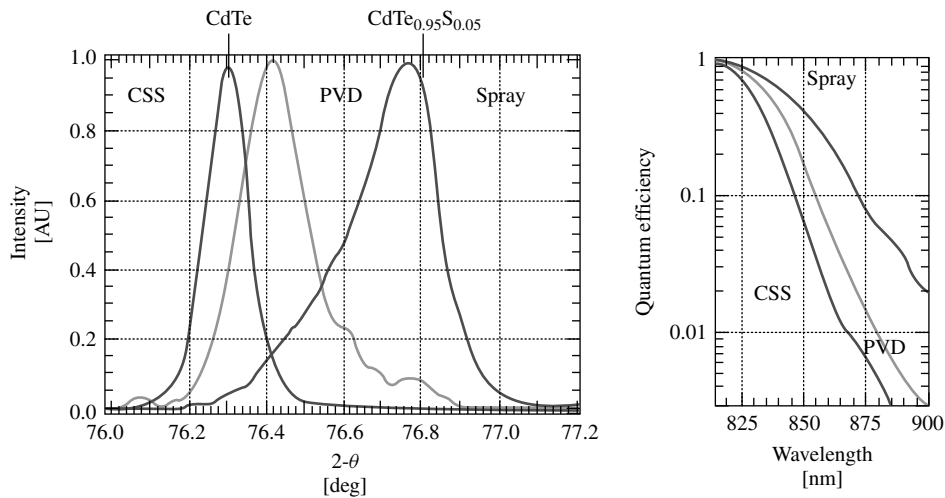


Figure 14.19 Correlation of XRD (511)/(333) reflection with long-wavelength quantum efficiency

copper-containing material. Copper will react with Te to form a p^+ -layer that can then be contacted with a metal or with graphite. The subtelluride Cu_2Te has been directly measured at the back surface using GIXRD methods [151]. Also, Cu acts as a relatively shallow donor in CdTe and can be diffused into CdTe from a doped contact material such as graphite paste [34] or ZnTe:Cu [205].

There are a variety of surface treatments that have been used, prior to formation of the copper layer, to reduce the back barrier. Table 14.3 gives a summary of these surface treatments and the corresponding materials that have typically been used for the back contact. Although fabrication laboratories tend to utilize a single surface treatment and contact material, there is little evidence that the preferred contact process is dependent on the deposition technique.

The high bulk-diffusion coefficient for Cu in CdTe, $3 \times 10^{-12} \text{ cm}^2/\text{s}$ at 300 K [156], coupled with its multiple valence states and weak Cu–Te bond give rise to potential stability issues related to its use as discussed below. Alternatives to the use of copper in the back

Table 14.3 Back-contact formation methods (NP = nitric + phosphoric acid mixture, BDH = sequential reaction in bromine, acidic dichromate, and hydrazine)

CdTe deposition method	Surface treatment	Primary contact	Thermal treatment	Additional contact	Reference
PVD	Te + H ₂	Cu	200°C/Ar	C	[152]
ED	BDH	Cu	None	Ni or Au	[153]
Spray	Etch	C + dopant	None	None	[154]
Screen	None	C + Cu dopant	400°C/N ₂	None	[155]
VTD	BDH	Cu	200°C/Ar	C	[151]
CSS	NP Etch	C + HgTe + Cu	200°C/He	Ag paste	[84]
Sputter	Br Etch	ZnTe:N	In situ	Metal	[156]
MOCVD	Br Etch	ZnTe:Cu	In situ	Metal	[157]

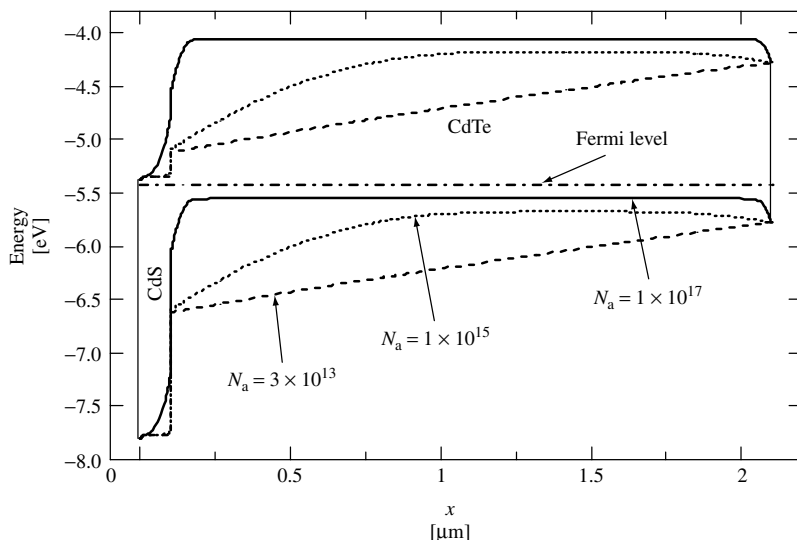


Figure 14.20 CdTe/CdS junction band diagrams at $V = 0$ for three values of CdTe acceptor density and a back-contact barrier = 0.3 eV

contact have generally involved the use of other tellurides, such as ZnTe:N [158] and Sb_2Te_3 [159], that can make reasonable contact to the CdTe and form only modest barriers with an appropriate metal. To date, however, contacts demonstrably free of Cu have not shown significant promise.

One consequence of a back-contact barrier, and the value of keeping it small, can be seen in the band diagrams of Figure 14.20 calculated by Alan Fahrenbruch for a 2- μm -thick CdTe layer [160]. The back contact is essentially a second diode with opposite polarity and smaller barrier than the primary junction. For a thick absorber, or one with reasonably large carrier density (solid curve), the bands are flat over most of the absorber thickness, the primary junction effectively blocks modest forward currents, and the back barrier has only a minor effect on the current–voltage curves. For carrier densities more typical of CdTe (between dashed and dotted lines), however, the depletion widths of the primary and back-contact diodes overlap. The effective reduction in the barrier for electrons means that forward current can flow more easily, reducing the open-circuit voltage.

14.3.5 Solar Cell Characterization

Considerable information about the electrical properties of CdTe solar cells has been deduced from straightforward measurements of current versus voltage (J – V), quantum efficiency (QE) and capacitance versus frequency (C – f) and voltage (C – V). More detailed information can be obtained from the temperature dependence or the time evolution of these curves.

The J – V curve (Figure 14.2) for the record-efficiency cell follows a standard diode equation with additional factors included to take account of circuit resistance and

forward-current mechanisms other than thermionic emission.

$$J = J_0 \exp[(V - JR)/AkT] - J_{SC} + V/r \quad (14.1)$$

For the illuminated J - V curves of the record-efficiency CdTe cell, the prefactor J_0 is 1×10^{-9} A/cm², the series resistance R is $1.8 \Omega\text{-cm}^2$, the diode quality factor A is 1.9, and the shunt resistance r is $2500 \Omega\text{-cm}^2$. The values for R and A were found using the technique described in Reference [161].

The forward-current ($J + J_{SC}$) data for the record-efficiency CdTe cell is replotted in Figure 14.21 using a logarithmic scale, and the analogous data of a high-efficiency GaAs cell [162] is shown for comparison. Since CdTe and GaAs have nearly the same band gap, they should ideally have the same lower limit to J_0 and same V_{OC} and J - V characteristic, if they were both limited by band-to-band recombination. Both curves have had small corrections for series and shunt resistances (R and r). Since the absorber materials have similar band gaps, the CdTe and GaAs cells should have similar J - V curves. The V_{OC} difference shown, however, is nearly 200 mV. At maximum power (MP), the voltage difference is larger yet, approaching 300 mV, because the CdTe A-factor is 1.9 compared to 1.0 for the GaAs. The physical difference is due to the additional recombination-current paths for the CdTe junction. This excess forward current for the CdTe cell is roughly two orders of magnitude greater than that of the GaAs cell under normal operating conditions. The implication is that there is considerable room for improvement of V_{OC} in CdTe cells through reduction in such recombination. Referring to the band diagrams in Figure 14.20, it is apparent that for sufficiently high density of midgap states, low doping levels in CdTe will enhance recombination current. Further, low doping levels and the resulting field profiles are expected to reduce minority transport, resulting in more pronounced voltage-dependent collection, reducing J_{MP} .

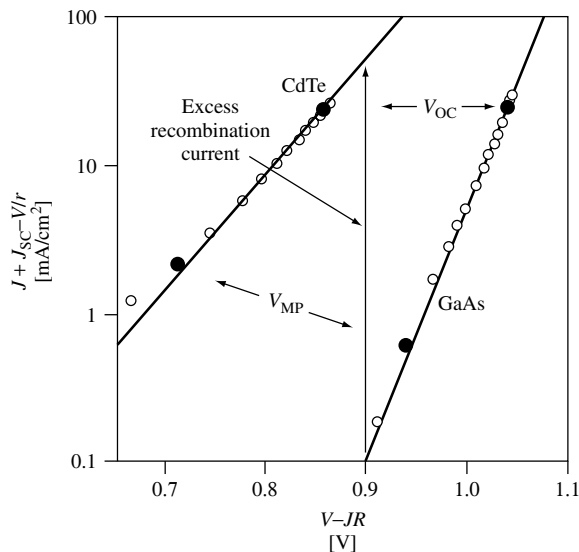


Figure 14.21 Comparison of high-efficiency CdTe and GaAs-illuminated J - V data on a log plot, corrected for resistive effects

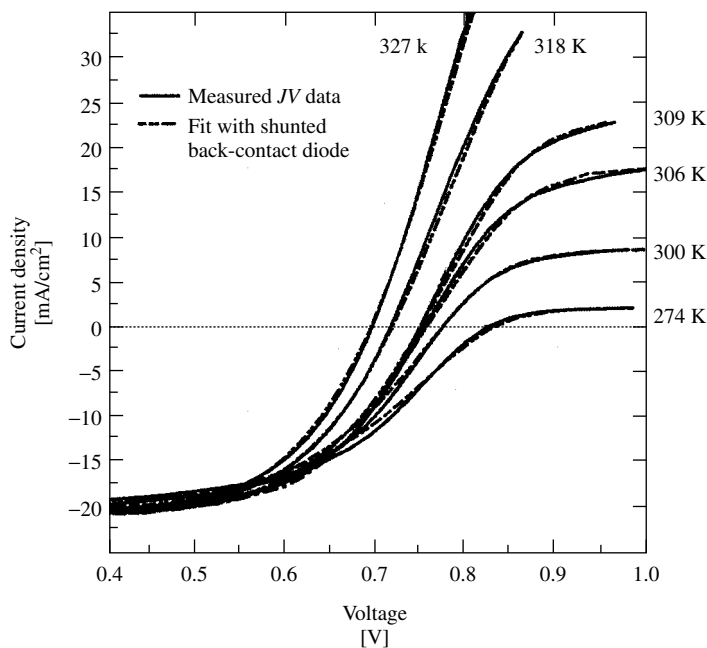


Figure 14.22 Measured and calculated curves for a CdTe cell with a back-contact barrier [162]

The effect of a back-contact barrier on the device band diagram was shown earlier in Figure 14.20. The effect on measured $J-V$ curves is illustrated in Figure 14.22. Assuming the two depletion regions do not overlap, the two diodes can be treated as independent circuit elements. The calculated fit to the curves, with a back-diode barrier height of 0.3 eV, is in fact quite good. The impact of the back barrier becomes larger as the temperature is lowered. This impact is very dramatic in the first quadrant, where the shape of the $J-V$ curves is commonly described as “rollover” [163–165]. The degree of “rollover” of $J-V$ curves such as those illustrated in Figure 14.22 has been shown to be related to the amount of copper used in the fabrication of the back contact [166]. With smaller amounts of copper, “rollover” is observed at higher temperatures implying a larger back-contact barrier, and it has a greater impact on cell performance.

The addition of large amounts of copper to reduce the back-contact barrier, and hence inhibit “rollover”, however, can lead to a decrease in CdTe cell stability, at least for cells held at elevated temperatures. Several authors have seen significant performance changes when CdTe cells were held at high temperatures (typically 60–110°C) for extended periods of time [167–171]. Such studies, often referred to as “stress” tests, generally first see a decrease in fill factor and next in V_{OC} . Only in extreme cases is J_{SC} affected. Figure 14.23 shows the illuminated $J-V$ curves for an NREL-manufactured CdTe cell soon after it was fabricated, and at different periods of time following light soaking at 100°C under open-circuit bias. Such curves are typical of those seen with cells from different manufacturers. The dark $J-V$ curves for these and other CdTe cells also show a progressive increase in “rollover” with continuing temperature stress. Qualitatively similar $J-V$ characteristics are measured for the devices of Figures 14.22 and 14.23,

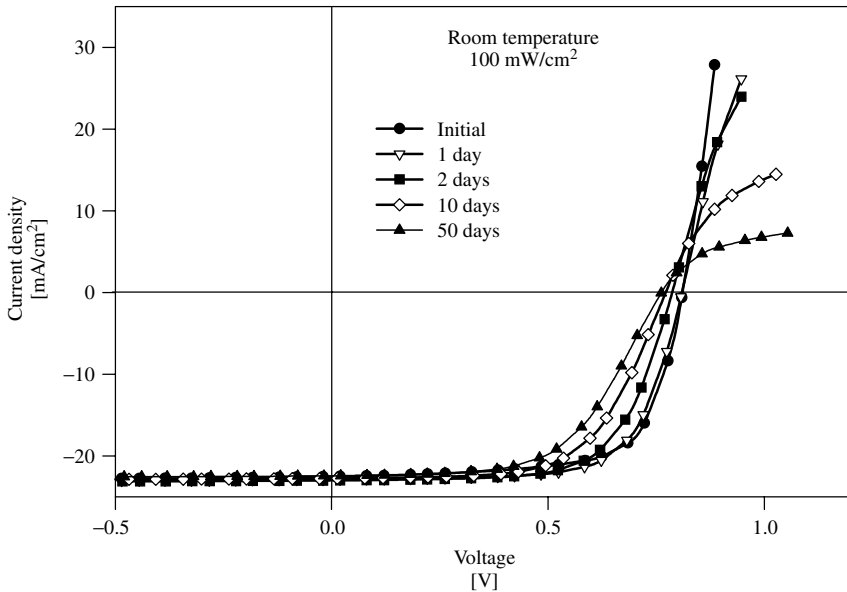


Figure 14.23 $J-V$ of CdTe cells following extended exposure to 100°C at V_{OC} [168]

showing an increase in rollover as temperature is decreased or as time at open-circuit 100°C stress is increased. As the temperature of the $J-V$ measurement is reduced, the acceptor concentration decreases, resulting in the back-barrier height exerting a greater effect, as shown in Figure 14.20. The rollover in the stressed devices could likewise be due to a reduction in carrier density in the CdTe layer.

There is conflicting evidence of the dependence of CdTe cell performance changes with stress temperature, but one study [169] has deduced an empirical activation energy near 1 eV, which predicts that $J-V$ changes at 100°C are accelerated 500 to 1000 times compared to a typical annual range of outdoor temperatures for solar panels. Hence, one would not expect significant performance changes for modules until they had been deployed in the field for many years.

Additional “stress” studies have shown that reductions in cell efficiency are smaller when the voltage bias is held at short circuit or maximum power, rather than at open circuit [169–171], or when less copper is used in the back contact [166]. The movement of copper out of the back-contact region is faster when forward bias reduces the electric field within the cell [169, 171–173], and it has at least two effects on cell performance. One is the increase in back-barrier height, similar to the copper-free case. The second is a detrimental effect on cell performance due to copper movement toward the front junction, probably enhanced by grain-boundary paths. There is no general agreement, however, on whether the copper causes an increase in CdTe recombination states, a change in the CdS layer, or possibly an increased overlap of the front and rear junctions by creating conducting filaments.

There are a variety of possible optical losses before the photons reach a CdTe solar cell’s absorber, and there are additional optical losses due to incomplete absorption of

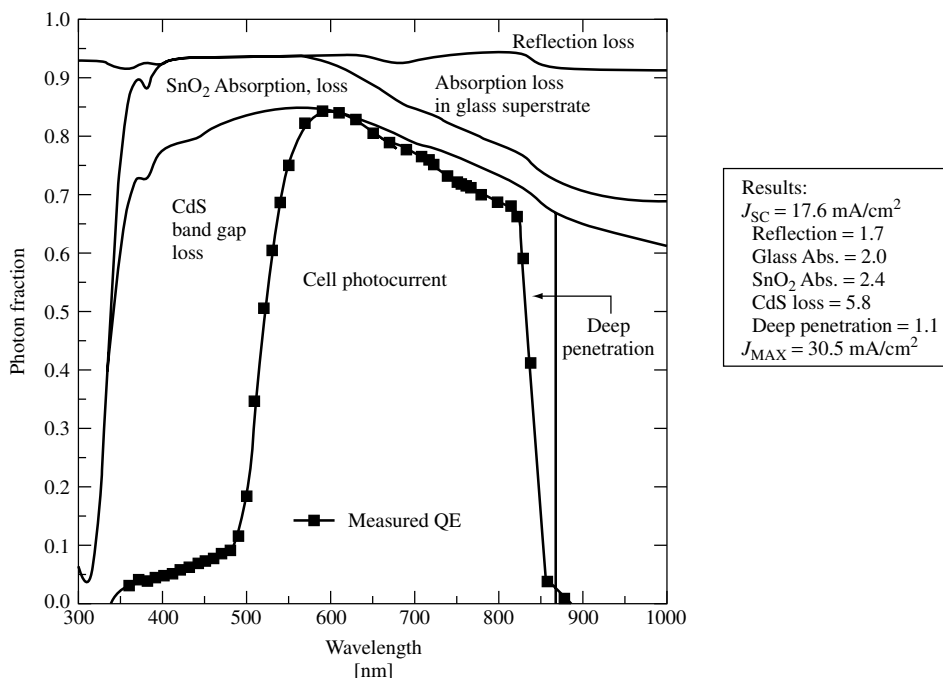


Figure 14.24 CdTe cell photon losses and quantum efficiency versus wavelength [174]

the photons penetrating through the absorber. The QE of a solar cell, especially when combined with independent reflection and absorption measurements of the cell and individual window layers, is a powerful tool to analyze these losses. The data shown in Figure 14.24 are for a CdTe cell with relatively large losses in J_{SC} . This cell, fabricated by Solar Cells, Inc., was deliberately chosen to illustrate the analysis process and is not indicative of the cells currently being manufactured.

To quantify the photon losses in Figure 14.21, the measured QE is multiplied by the light spectrum, in units of photons/cm²/nm, integrated over wavelength, and multiplied by unit electric charge to yield J_{SC} . For comparison, the maximum current density J_{max} is found to be 30.5 mA/cm² for $E_g = 1.5$ eV by a similar calculation up to the band gap cutoff wavelength (vertical line) using unity QE.

The optical regions shown in Figure 14.24 are the reflection from the cell, the absorption of the glass superstrate, the absorption of the SnO₂ conductive contact, and the loss below 500 nm associated primarily with absorption of a ~250-nm-thick CdS window. The separation of individual absorption terms was deduced from the reflection and transmission of partially completed cell structures terminated after each layer. The remaining loss region approaching the band gap is assumed to be due to the photons that penetrated too deeply for complete collection. Integration of these loss spectra, again weighted by the illumination spectrum, gives the current-density loss for each. These losses are listed in the inset to Figure 14.24 for the standard global AM1.5 spectrum [175], normalized to 100 mW/cm². The sum of the losses is the difference between the measured and the maximum current densities.

The inset tells us quantitatively that considerable current enhancement is possible by employing a thinner CdS window, and to a lesser extent with a different glass or improved SnO_2 process. Potential for improvement in J_{SC} with an antireflection coating or from better collection of the deeply penetrating photons would be even smaller. It is certainly possible, however, to reduce the larger losses. The record efficiency cell, for example, has a J_{SC} of 26 mA/cm^2 . Its losses from glass, SnO_2 , and CdS absorption are each more than a factor of five less than the cell shown in Figure 14.23, and no single loss factor contributes more than 1 mA/cm^2 .

The capacitance of a solar cell can yield information about extraneous states within the band gap, and it can often give a credible profile of the carrier density within the absorber [176]. Figure 14.25(a) shows the measured capacitance of a CdTe cell as a function of frequency for three biases: 0, -1 , and -3 V . The capacitance magnitude is relatively small, corresponding to a small carrier density and a large depletion width. The large depletion width implies that most photons are absorbed in a region with an electric field and hence photocurrent does not vary significantly with voltage [177]. The fact that the curves are relatively flat over nearly three decades in frequency strongly suggests that they are not significantly affected by extraneous states. The upturn at high frequencies is

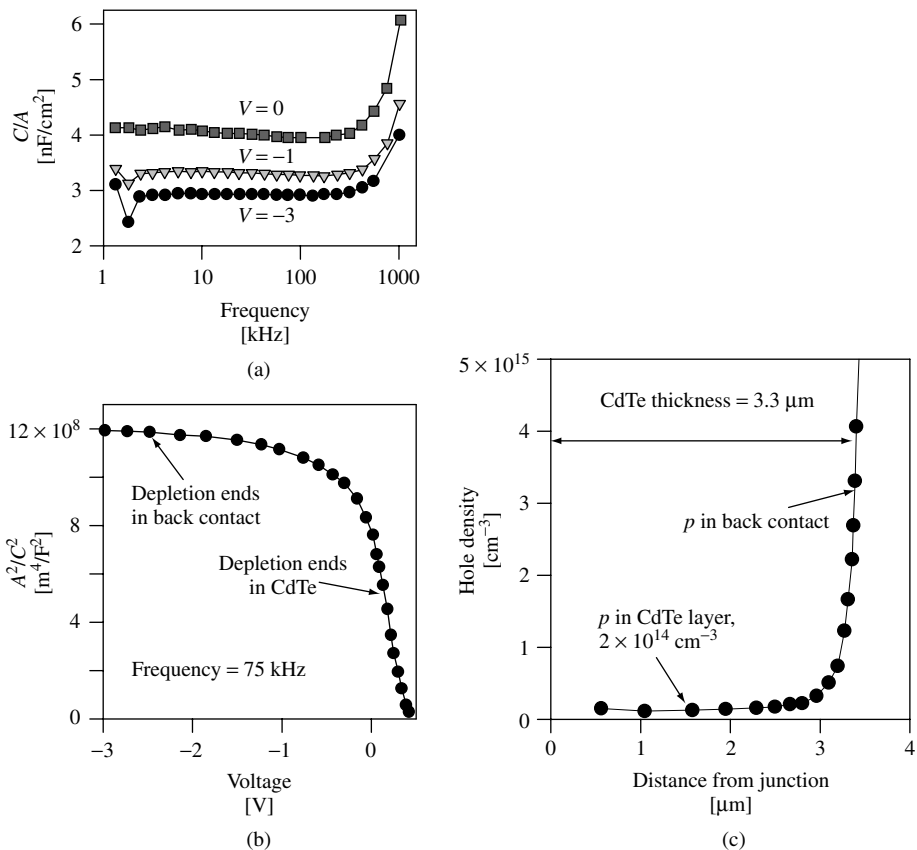


Figure 14.25 Capacitance measurements and hole-density determination for a CdTe solar cell

due to circuit inductance [178], and the points off the curves at low frequencies are due to an apparatus anomaly. Typically, a frequency in the middle of the flat region, in this case 75 kHz, is chosen for subsequent $C-V$ measurements.

Capacitance versus voltage data at 75 kHz is plotted in Figure 14.25(b) in the commonly used C^{-2} versus V format, in which the vertical axis is proportional to the square of the depletion width, w , for a given voltage, since $C/A = \epsilon/w$. The slope is inversely proportional to the carrier density at the depletion edge. In this case, there are two distinct regions. In reverse bias, the C^{-2} , and hence the depletion width, changes very little. Near zero bias and into forward bias, however, the depletion width narrows considerably.

The same data can be plotted (Figure 14.25c) as hole density ρ versus depletion width, which is referred to as the distance from the junction, since the depletion is assumed to be essentially all in the absorber. The two regions suggested by the C^{-2} versus V plot have become extremely clear. For the first 3 μm into the CdTe, the hole density is very low (mid 10^{14} range), but then it increases dramatically. The interpretation is that 3 μm is the thickness of the CdTe layer, and the rapid increase in hole density takes place as the depletion edge enters the back-contact region. In fact, the measured thickness of this particular CdTe was somewhat larger than 3 μm , and in general the electronic thickness is comparable to the physical thickness. The likely explanation is that there are local areas such as grain boundaries and highly defective grains where the back-contact material penetrates into the CdTe and effectively reduces its thickness. Following the elevated temperature cycles that led to Figure 14.23, there can also be a reduction in net CdTe thickness.

CdTe solar cells fabricated by a variety of the techniques illustrated in Figure 14.6 have shown hole densities between 1×10^{14} and $8 \times 10^{14}/\text{cm}^3$ as determined by the capacitance technique. A relatively low carrier density may be an impediment to higher-efficiency cells. It suggests that compensating native donors remain a problem for the CdTe cells made to date. The direct impact of the low hole density is that the Fermi level is 250 to 350 mV from the valence-band maximum, and hence limits the junction barrier, and therefore V_{OC} . A bigger, and probably related, problem is that the low densities are likely to be symptomatic of the excessive recombination states responsible for much of the voltage and fill-factor difference seen in Figure 14.21.

14.3.6 Summary of CdTe-cell Status

During the past 20 years, there has been major progress in refining the basic CdTe cell structure of Bonnet and Rabenhorst. The highest current densities achieved are similar to crystalline GaAs when adjusted for small differences in band gap. Open-circuit voltage and fill factor are limited by excessive forward-current recombination and low carrier density, but have nevertheless achieved values about 80% as large as GaAs, again adjusted for band gap. The recombination current appears to follow the Shockley–Read–Hall mechanism through distributed states in the space charge region [179]. There is some concern about the diffusion of copper atoms, but significant degradation under normal operating conditions for well-fabricated cells is unlikely. Although cell-level basic research should certainly continue, the status of CdTe solar cells is clearly healthy enough to proceed with mainstream commercialization.

14.4 CdTe MODULES

A CdTe photovoltaic module consists of electrically interconnected CdTe cells on a superstrate that serves as the mechanical support. The module's electrical output depends on individual cell output, interconnection scheme, and losses due to nongenerating areas and interconnection-resistive losses. Obtaining high cell efficiency at the module scale depends on the successful transfer of small-area batch processing steps, such as the CdCl_2 treatment, to either large-area batch or continuous processing, and on minimizing dead-area and resistive losses as well as optical losses due to the use of low-cost glass. In effect, the manufacturer's goal is to obtain a series-connected array of large-area CdTe/CdS diodes having spatially uniform physical and electrical properties in a high-throughput fabrication process. This manufacturing orientation is somewhat different from that of integrated-circuit manufacturers, where the challenge lies in minimizing the spatial dimension of each circuit element.

The electrical interconnections between adjacent cells can be made via external contacts or by monolithic integration during deposition and processing. For cost-effective commercial-scale modules, the principle of monolithic integration is often adopted, where the cells on a single large-area substrate or superstrate are isolated and interconnected by scribing through the deposited layers at different stages of fabrication. Scribing can be achieved by mechanical means or, preferably, by laser scribing in which the stopping point is determined by matching the absorption properties of the different layers with the appropriate wavelength and power density [180]. The first scribe isolates the TCO front contact, the second through the CdS and CdTe provides an electrical path from the TCO to the back contact of an adjacent cell, and the third isolates the back contact between cells. A monolithically interconnected module is shown in Figure 14.26. The photocurrent generated by each individual cell flows from one end of the module to the other. The module voltage is simply the sum of the voltages from the series connected individual cells. This monolithic structure and its three laser scribes are very similar to that of amorphous silicon-based PV modules. Significant design analysis of module geometry and lateral-sheet resistances, to minimize resistive and dead-area losses, has been carried out for amorphous silicon PV modules, and is applicable to CdTe PV modules [181, 182].

The structure shown in Figure 14.26 utilizes a sheet of glass as the supporting superstrate. The choice of glass is based on the cost per watt, optical loss, and thermal

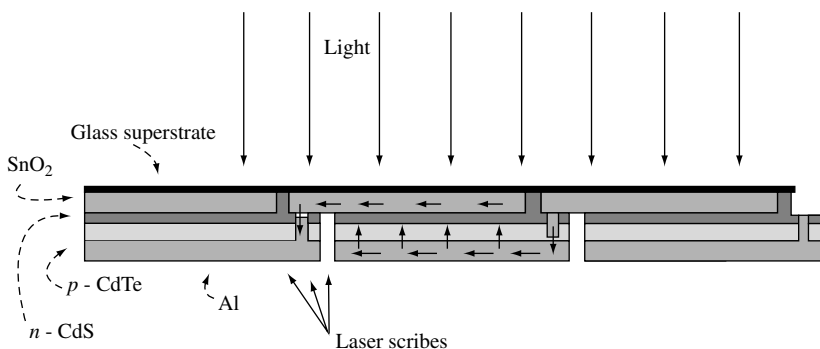


Figure 14.26 Schematic of a series-connected integrated CdTe module having three laser scribes

tolerance of the glass. For example, the light-generated current in CdTe cells deposited on borosilicate glass is 2 mA/cm² higher than on soda lime glass, owing to high absorption in the soda lime glass above 600 nm. However, the high-transparency glasses, such as borosilicates, fused quartz, and Vycor, require more refining and are thus significantly more costly than the soda lime glass commonly used for windowpanes. A review of the optical properties of these and other glasses is found in Reference [183]. In addition, low-cost soda lime glass exhibits a lower softening temperature, restricting its application for high-temperature processing. Reducing the iron content in soda lime glasses improves the transparency at wavelengths greater than 600 nm and raises the melt temperature, at a lower cost than borosilicate or other highly refined glass types.

Commercialization of CdTe PV modules will rely on a constant supply of affordable raw materials, especially cadmium and tellurium. In terms of the material requirements, a facility with 1 MW/year manufacturing capacity, with 100% utilization of Cd and Te species using a 2- μ m-thick absorber layer, will require approximately 1 metric tons of CdTe, which translates to 0.4 metric ton of cadmium and 0.6 metric ton of tellurium. Both elements are obtained as the by-products in the smelting of ores; cadmium is obtained from zinc, copper, and lead refining, while tellurium is primarily obtained as a product of the electrolytic refining of copper and skimmings from lead production [184]. Tellurium is the scarcer and more costly component, however, tellurium availability is estimated to be \sim 1600 metric tons per year [185]. At present, the costs for \sim 95% pure cadmium and tellurium are \sim \$US 12/lb (\$US 24 000/ton) and \sim \$US 20/lb (\$US 40 000/ton), respectively. Thus, the total cadmium and tellurium costs for the 1-MW capacity plant would be \sim \$US 34 000, which amounts to less than \$US 0.10 per watt. This is significantly less than the price of the superstrate glass/TCO for the 100 000 m² required for 1-MW capacity, which is currently \$US 10.80/m² [186], equaling \$US 1.08 per watt. A detailed analysis of PV-manufacturing costs is presented in Reference [187].

Present-generation CdTe PV modules are typically \sim 1 m² in area and have achieved efficiencies above 10%, with peak power on the order of 90 W. At the time of this writing, the only commercial CdTe cells are manufactured by Matsushita Battery Company in Japan, with an annual production of 1.2 MW [188]. Three CdTe module manufacturers are entering production: First Solar, L.L.C., in Toledo, Ohio; BP Solar, in Fairfield, California; and Antec Solar GmbH, in Germany. The module dimensions and output of prototype superstrate CdTe modules from these companies are listed in Table 14.4.

The First Solar module utilizes vapor transport deposition of CdTe onto moving substrates to achieve a high growth rate while maintaining high substrate temperature. The

Table 14.4 Summary of CdTe module performance, compiled by Zweibel. Consult the listed references for module fabrication details

Manufacturer	Country	CdTe method	Per-module power [W]	Aperture efficiency [%]	Module size [m ²]	Reference
Antec	Germany	CSS	47	7.0	0.66	[189]
BP Solar	USA	ED	92	11.0	0.84	[4]
First Solar	USA	VTD	67	10.1	0.66	[3]
Matsushita	Japan	Screen	59	11.0	0.54	[190]

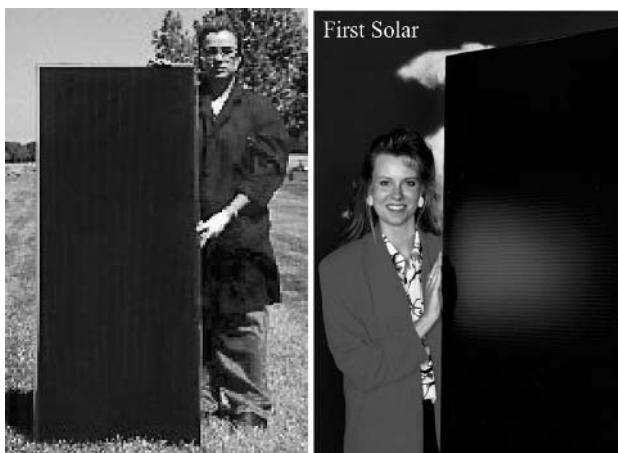


Figure 14.27 CdTe modules made by (a) BP Solar and (b) First Solar. (BP Solar photograph courtesy of D. Cunningham. First Solar photograph courtesy D. Rose)

modules are formed on tin oxide-coated soda lime glass made by Libby Owens Ford. The production line is reported to be capable of 2.9 m^2 per minute throughput [191]. A photograph showing a First Solar module is shown in Figure 14.27(b).

The BP Solar module utilizes electrodeposited CdTe films and overcomes throughput issues associated with low growth rate by simultaneous batch deposition of many modules. The plant has eight identical reaction chambers, or tanks. Each tank is capable of handling 40, 0.55 m^2 ($14'' \times 61''$) substrates or 24, 0.94 m^2 ($24'' \times 61''$) substrates [192]. A photograph of a BP Solar module is shown in Figure 14.27(a).

The Antec module utilizes CSS deposition of the CdTe layer, with a patented source diffuser to improve spatial uniformity during deposition. Spatial uniformity in CSS deposition is an issue because the source and substrate have the same area and are in static relation to each other.

Issues confronting manufacturers of thin-film CdTe solar cells are maintaining small-area efficiencies at the module scale, control of uniformity during growth, reproducibility, and product certification with respect to expected lifetime. Module performance and spatial uniformity are linked to the CdS film thickness; thick CdS films improve processing latitude but reduce light-generated current. With the ultrathin CdS films used to obtain state-of-the-art performance in small-area cells, spatial variations in CdTe-film microstructure can affect the diffusion of CdS into CdTe and the resulting junction structure. Incorporating buffer layers into the window-layer side of the structure, refining the postdeposition treatments, and developing in-line sensing diagnostic tools are viable pathways for widening the tolerance window needed to raise the current density in modules.

14.5 THE FUTURE OF CdTe-BASED SOLAR CELLS

The future of CdTe thin-film photovoltaic devices in energy production and optical sensing is assured by the material properties, laboratory-scale device performance, and photovoltaic module implementation. Enhancing the viability of CdTe/CdS for terrestrial

power generation depends on improving device performance, cost-effective translation of fabrication processes to the module scale, and cell and module stability. In addition to efficiency gains in single-junction devices, band gap tailoring of the absorber by alloying with other group IIB metals can facilitate development of multijunction cells with efficiencies approaching 30%. Translating single-junction efficiency gains from batch processes to continuous module fabrication and developing monolithic multijunction modules on a single superstrate can significantly reduce production costs. Achieving this goal requires greater understanding of the relationship between processing conditions and critical material properties needed for high efficiency and good long-term stability.

Although the fundamental nature of polycrystalline CdTe is not yet fully understood, we have shown that significant progress has been made toward the development of 20% efficient single-junction thin-film cells. In addition, we have seen that several CdTe film deposition techniques yield similar device performance, by a suitable combination of postdeposition processing and back-contact formation. Reaching the 20% efficiency target and translating this to high module performance relies on determining and overcoming the mechanisms that limit the open-circuit voltage and fill factor in present-generation cells. This is simply due to the fact that the current density in champion thin-film CdTe cells has reached 80% of its theoretical maximum for AM1.5 illumination and is primarily limited by optical losses in the glass/TCO/CdS structure. The values of $V_{OC} \sim 850$ mV and $FF \sim 75\%$ appear to represent practical limits, and fall short of the expectations based on band gap. Forward current in present-generation high-efficiency CdTe/CdS devices appears to be controlled by the Shockley–Read–Hall recombination in the space charge region. Many investigations also show a profound influence of back-contact formation on both V_{OC} and FF . For module implementation, obtaining both high J_{SC} and V_{OC} is complicated by large-area control of CdTe–CdS interdiffusion and junction formation between the CdTe absorber and the TCO, since a thin CdS layer is required in the finished device. Thus, critical research directions for improving efficiency in CdTe/CdS cells are (1) identification and reduction of the density of limiting intragrain defect states; (2) increasing the p -type carrier concentration in CdTe; (3) eliminating or controlling parallel junctions that may arise because of pinholes; (4) developing robust manufacturing processes; and (5) defining and overcoming performance limitations related to back-contact formation.

In addition to its basis for single-junction devices, CdTe can be alloyed with other II^B-VI^A compounds to alter its band gap, allowing multijunction cells to be designed. The multijunction cell structures using CdTe-based wide band gap cells in monolithic structures must confront the relationship between cell geometry and both processing temperature and chemical stability. Materials based on alloys between CdTe and other group II^B-VI^A compounds allow a wide range of optoelectronic properties to be incorporated into devices by design.

Semiconducting compounds of the form II^B-VI^A provide a basis for the development of tunable materials, obtained by alloying different compounds in pseudobinary configurations. For photovoltaic heterojunction devices, semiconductors using Cd, Zn, Hg cations and S, Se, Te anions exhibit a wide range of optical band gap, suggesting their potential for use in optimized device designs by tailoring material properties (Table 14.5). The high optical absorption coefficients, $\sim 10^5/\text{cm}$, and direct optical band gaps of many $II-VI$ semiconductors make them suitable for use in thin-film photovoltaic

Table 14.5 Properties of pseudobinary II^B-VI^A alloys suitable for absorber layers

Compound	Single crystal optical E_g range 300 K [eV]	Optical bowing parameter	Stable endpoint structure	Miscibility gap?
Cation substitution				
$\text{Cd}_{1-x}\text{Zn}_x\text{Te}$	1.49–2.25	0.20	ZB–ZB	N
$\text{Hg}_{1-x}\text{Cd}_x\text{Se}$	0.10–1.73	?	ZB–W	N
$\text{Hg}_{1-x}\text{Zn}_x\text{Te}$	0.15–2.25	0.10	ZB–ZB	N
Anion substitution				
$\text{CdTe}_{1-x}\text{S}_x$	1.49–2.42	1.70	ZB–W	Y
$\text{CdTe}_{1-x}\text{Se}_x$	1.49–1.73	0.85	ZB–W	?
$\text{CdSe}_{1-x}\text{S}_x$	1.73–2.42	0.31	W–W	N
$\text{HgTe}_{1-x}\text{S}_x$	0.15–2.00	?	ZB–ZB	?
$\text{HgSe}_{1-x}\text{S}_x$	0.10–2.00	?	ZB–ZB	?

devices. For terrestrial photovoltaic applications, in which a band gap of ~ 1.5 eV is desired, considerable progress has been made in the development of solar cells based on the CdS–CdTe heterojunction wherein $\text{CdS}_{1-y}\text{Te}_y$ and $\text{CdTe}_{1-x}\text{S}_x$ alloys have been shown to play a role in the device operation. For the development of next-generation, multijunction cells, top cells with an absorber band gap of ~ 1.7 eV are required [193, 194].

The alloy systems shown in Table 14.5, separated by cation and anion substitution in pseudobinary compounds, define a broad range of optical band gap suitable as absorber layers in terrestrial photovoltaic converters. The isostructural systems $\text{Cd}_{1-x}\text{Zn}_x\text{Te}$ and $\text{Hg}_{1-x}\text{Zn}_x\text{Te}$ offer tunable systems with a wide range of band gap and controllable p -type conductivity.

Thin-film solar cells based on $\text{Cd}_{1-x}\text{Zn}_x\text{Te}$ were the subject of study in the late 1980s, by several laboratories, including the Georgia Institute of Technology (GIT) and International Solar Energy Technology (ISET). Two approaches to depositing the $\text{Cd}_{1-x}\text{Zn}_x\text{Te}$ films had been considered in the previous work: synthesis by reaction of sequentially deposited metal layers (ISET) and metal organic chemical vapor deposition (GIT). CdS/ $\text{Cd}_{1-x}\text{Zn}_x\text{Te}$ devices using $\text{Cd}_{1-x}\text{Zn}_x\text{Te}$ films made by the reaction of sequentially deposited metals with $x = 0.1$, corresponding to $E_g \sim 1.6$ eV, yielded 3.8% efficiency and suffered from low V_{OC} and FF [195]. Although little follow-up work was conducted to explain the low performance, for CdS/ $\text{Cd}_{1-x}\text{Zn}_x\text{Te}$ devices made by MOCVD, it was found that the CdCl_2 + air treatment step reduced the band gap from 1.7 to 1.55 eV, owing to chemical conversion of the zinc alloy to volatile ZnCl_2 . The best cells made with the 1.55 eV band gap yielded 4.4% conversion efficiency [196].

CdTe-based thin-film photovoltaic devices are also suited to applications beyond terrestrial power conversion, including space-power generation, infrared detectors, and gamma radiation detectors. Using the current–voltage characteristics of state-of-the-art and realistic devices on rigid glass superstrates, AM0 operation at 60°C can be determined by accounting for the temperature dependence of the band gap and differences in irradiance. State-of-the-art cells with 16.5% AM1.5 efficiency at 25°C translate to 13.9% AM0 efficiency at 60°C . Typical cells having 12% AM1.5 efficiency at 25°C

translate to 10% AM0 efficiency at 60°C. For cells on 0.05-mm-thick polyimide substrate at AM0 conditions, the 12% state-of-the-art and 10% typical cells should yield power-to-weight ratio of 1520 and 1100 W/kg, respectively. CdTe research and development for space applications, in which AM0 power-to-weight ratio greater than 1000 W/kg is desired, has followed three approaches with results as follows: (1) 6 to 7% AM1.5 efficiency for thin-film deposition in the *substrate* configuration on lightweight flexible substrates [25], (2) 11% AM1.5 efficiency for transfer of completed superstrate cells from rigid superstrates to lightweight flexible substrates [197], and (3) 11% efficiency for direct superstrate deposition onto 100- μm thick glass foils [105]. Encouraging results of CdTe/CdS cell stability were obtained under 1-MeV electron bombardment at fluences of 10^{14} to $10^{16}/\text{cm}^2$ [198].

For infrared detection and thermal imaging, devices using $\text{Cd}_{1-x}\text{Hg}_x\text{Te}$ alloys have been investigated intensively since the mid 1960s, leading to a significant technology base of sensor and charge-coupled device (CCD) imaging devices [199]. To achieve good sensitivity at wavelengths of 8 to 10 μm , long minority-carrier lifetime is required in the absorbing $\text{Cd}_{1-x}\text{Hg}_x\text{Te}$. To minimize trapping and Shockley–Read–Hall recombination centers, single crystals are fabricated using either a cast-recrystallization technique or the Bridgman growth technique. Schottky photodetecting arrays are fabricated on polished slices of the single crystals. High-quality $\text{Cd}_{1-x}\text{Hg}_x\text{Te}$ thin films have been deposited by both liquid-phase and vapor-phase epitaxy on CdTe and $\text{Cd}_{1-x}\text{Hg}_x\text{Te}$ single-crystal wafers [200].

Gamma ray detectors for tomographic applications based on CdTe have been investigated using two approaches: (1) direct detection by ionization in CdTe and (2) deposition of a CdTe/CdS thin-film photodetector on a scintillating superstrate such as cadmium tungstenate (CdWO_4). For direct detection, the gamma ray is stopped in CdTe in either a metal–semiconductor–metal or all-semiconductor *p-i-n* structure using CdTe single crystals [201]. In either design, the optimal detector is achieved with devices having the lowest possible leakage current and highest mobility-lifetime product.

Concerns have been raised about cadmium toxicity and the possibility of introducing significant amounts into the environment where the cells are manufactured and deployed. Managing cadmium in the manufacturing environment relies on a combination of appropriate engineering and chemical hygiene practices. Concerns over module deployment are being addressed at technical and policy levels. First, modules are environmentally well sealed, which serves to both protect the cell from environmental deterioration and to contain the semiconducting materials, in the event of mechanical failure. By recycling modules at the end of life in a manner consistent with metal products, it is estimated that nearly all the cadmium in a module can be recycled at a cost of roughly 5 cents/W [202]. Alternatively, module deployment by a leasing arrangement or by confinement to industrially managed energy farms could facilitate total control over installed cadmium distribution. The amount of cadmium used in thin-film CdTe modules is relatively modest. A CdTe module 1 m^2 in area, producing approximately 100 W of power using a CdTe layer less than 2 μm thick, contains less than 10 g of cadmium, or about the same as a single nickel–cadmium flashlight battery [203]. On a larger scale, it would take about 40 000 metric tons of cadmium to switch the entire US power grid to CdTe modules. Assuming a 30-year life cycle, about 7% of the current world output of cadmium would be required.

This chapter has shown the development and present state of CdTe solar cells and modules. Wide-scale commercialization of CdTe technologies hinges on improving performance, understanding stability, developing low-cost consumer products for varying energy and photonic market demands, and managing cadmium. At the cell level, improved performance can be expected as fundamental understanding of the device operation improves. Issues related to stability involve both cell-related mechanisms, linked to cell processing, and module-related mechanisms, linked to encapsulation and environmental conditions. Future CdTe product development hinges on successful marketing of photovoltaics as a viable energy source, which in turn depends on reductions in the cost per installed watt, which, at the time of this writing, makes thin-film CdTe solar cells a leading contender for future power generation.

14.6 ACKNOWLEDGMENTS

Brian McCandless wishes to acknowledge the contributions of the technical staff at the Institute of Energy Conversion, in particular Robert Birkmire, James Phillips, and Steven Hegedus for insightful discussions; Kevin Dobson and Joy Deep Dass for assistance in literature research; and Shannon Fields and Erten Eser for help with figure preparation. James Sites is deeply indebted to many colleagues in the CdTe community, but particularly to the students who have done research with him in this area: Pete Mauk, Hossein Tavakolian, Rick Sasala, Ingrid Eisgruber, Gunther Stollwerck, Nancy Liu, Jennifer Granata, and Jason Hiltner. Both authors gratefully acknowledge long-time research support from the United States National Renewable Energy Laboratory. The comparative nature of this work would not have been possible without access to samples and data generously provided by numerous CdTe research groups.

REFERENCES

1. Loferski J, *J. Appl. Phys.* **27**, 777–784 (1956).
2. Based on Rothwarf A, Boer K, *Prog. Solid. State Chem.* **10**, 71–102 (1975).
3. Frerichs R, *Phys. Rev.* **72**, 594–601 (1947).
4. Jenny D, Bube R, *Phys. Rev.* **96**, 1190–1191 (1954).
5. Krüger F, de Nobel D, *J. Electron.* **1**, 190–202 (1955).
6. de Nobel D, *Philips Res. Rpts* **14**, 361–399 and 430–492 (1959).
7. Rappaport P, *RCA Rev.* **20**, 373–397 (1959).
8. Mimilya-Arroyo J, Marfaing Y, Cohen-Solal G, Triboulet R, *Sol. Energy Mater.* **1**, 171 (1979).
9. Cohen-Solal G, Lincot D, Barbe M, Conf. Rec. 4th ECPVSC, 621–626 (Stresa, Italy, 1982).
10. Fahrenbruch A, Bube R, *Fundamentals of Solar Cells*, Academic Press, New York, 418–460 (1983).
11. Elliot J, Ed, US Air Force ASD Technical Report 61–242 (1961).
12. Cusano D, General Electric Res. Lab. Report, No. 4582 (1963).
13. Bernard J, Lancon R, Paparoditis C, Rodot M, *Rev. Phys. Appl.* **1**, 211–217 (1966).
14. Lebrun J, Conf. Rec. 8th IEEE Photovoltaic Specialist Conf., 33–37 (1970).
15. Justi E, Schneider G, Seredynski J, *J. Energy Conversion* **13**, 53–56 (1973).
16. Ponpon J, Siffert P, *Rev. Phys. Appl.* **12**, 427–431 (1977).
17. Fulop G *et al.*, *Appl. Phys. Lett.* **40**, 327–328 (1982).
18. Mitchell K, Fahrenbruch A, Bube R, *J. Appl. Phys.* **48**, 829–830 (1977).
19. Nakazawa T, Takamizawa K, Ito K, *Appl. Phys. Lett.* **50**, 279–280 (1987).

20. Aranovich J, Golmayo D, Fahrenbruch A, Bube R, *J. Appl. Phys.* **51**, 4260–4265 (1980).
21. Muller R, Zuleeg R, *J. Appl. Phys.* **35**, 1550–1556 (1964).
22. Dutton R, *Phys. Rev.* **112**, 785–792 (1958).
23. Mitchell K, Fahrenbruch A, Bube R, *J. Appl. Phys.* **48**, 4365–4371 (1977).
24. Yamaguchi K, Matsumoto H, Nakayama N, Ikegami S, *Jpn. J. Appl. Phys.* **16**, 1203–1211 (1977).
25. McClure J *et al.*, *Sol. Energy Mater. Sol. Cells* **55**, 141–148 (1998).
26. Adirovich E, Yuabov Y, Yugadaev D, *Sov. Phys. Semicond.* **3**, 61–65 (1969).
27. Bonnet D, Rabenhorst H, Conf. Rec. 9th IEEE Photovoltaic Specialist Conf., 129–132 (1972).
28. Phillips J *et al.*, *Phys. Status Solidi (B)* **194**, 31–39 (1996).
29. Suyama N *et al.*, Conf. Rec. 21st IEEE Photovoltaic Specialist Conf., 498–503 (1990).
30. Başol B, Conf. Rec. 21st IEEE Photovoltaic Specialist Conf., 588–594 (1990).
31. Tyan Y, Perez-Albuerne E, Proc. 16th IEEE Photovoltaic Specialist Conf., 794–800 (1982).
32. Meyers P, Liu C, Frey T, U.S. Patent 4,710,589 (1987).
33. Birkmire R, Conf. Record NREL ARD Rev. Meeting, 77–80 (1989).
34. Britt J, Ferekides C, *Appl. Phys. Lett.* **62**, 2851–2852 (1993).
35. Wu X *et al.*, *J. Appl. Phys.* **89**, 4564–4569 (2001).
36. McCandless B, Hichri H, Hanket G, Birkmire R, Conf. Rec. 25th IEEE Photovoltaic Specialist Conf., 781–785 (1996).
37. Wu X *et al.*, Conf. Rec. 17th European Photovoltaic Solar Energy Conversion 995–1000 (2001).
38. Mitchell K, Fahrenbruch A, Bube R, *J. Appl. Phys.* **48**, 829–830 (1977).
39. Rakhshani A, *J. Appl. Lett.* **81**, 7988–7993 (1997).
40. Fardig D, Masters Thesis, University of Delaware, Department of Electrical Engineering (1991).
41. Fahrenbruch A, Colorado State University subcontract report (2000), unpublished.
42. Hartmann H, Mach R, Selle B, “Wide Gap II-VI Compounds as Electronic Materials”, in Kaldis E, Ed, *Current Topics in Materials Science*, Vol. 9, North-Holland Publishing Company, New York (1982).
43. Madelung O, *Semiconductors Other than Group IV Elements and III-V Compounds*, Springer-Verlag, New York (1992).
44. Aven M, Prener J, Eds, *Physics and Chemistry of II-VI Compounds*, John Wiley and Sons, New York, 211–212 (1967).
45. International Committee for Diffraction Data, Card Number 15–770.
46. Knacke O, Kubaschewski O, Hesselmann K, *Thermochemical Properties of Inorganic Substances*, 2nd Edition, Springer-Verlag, New York (1991).
47. Data from ASM Binary Phase Diagrams (2000).
48. Data from Knacke O, Kubaschewski O, Hesselmann K, *Thermochemical Properties of Inorganic Substances*, 2nd Edition, Springer-Verlag, New York (1991).
49. Hultgren R *et al.*, *Selected Values of the Thermodynamic Properties of Binary Alloys*, American Society for Metals, Ohio, 627–630 (1971).
50. de Nobel D, *Philips Res. Rpts* **14**, 361–399 and 430–492 (1959).
51. Krüger F, *Revue de Physique Appliquée* **12**, 205–208 (1977).
52. Wei S, Zhang S, Zunger A, *J. Appl. Phys.* **87**, 1304–1311 (2000).
53. Phillips J, *Bonds and Bands in Semiconductors*, 42, Academic Press, New York (1973).
54. Huheey J, Keiter E, Keiter R, *Inorganic Chemistry*, 113–126, Harper Collins, New York (1993).
55. Wu W, Gielisse P, *Mater. Res. Bull.* **6**, 621–638 (1971).
56. Myers T, Edwards S, Schetzina J, *J. Appl. Phys.* **52**, 4231–4237 (1981).
57. Wei S, Zunger A, *Appl. Phys. Lett.* **72**, 2011–2014 (1998).
58. Cohen M, Bergstresser T, *Phys. Rev.* **141**, 789–801 (1966).
59. Wei S, Zhang S, Zunger A, *J. Appl. Phys.* **87**, 1304–1310 (2000).

60. Wei S, Mtg. Record, National CdTe R&D Team Meeting (2001) Appendix 9.
61. Başol B, *Int. J. Sol. Energy* **12**, 25–35 (1992).
62. Capper P, Ed, *Properties of Narrow Gap Cadmium-Based Compounds*, INSPEC, London, 472–481 (1994).
63. Kazmerski L, *Sol. Cells* **24**, 387–418 (1988).
64. Mueller K, *Thin Solid Films* **174**, 117–132 (1989).
65. Levi D *et al.*, *Sol. Energy Mater. Sol. Cells* **41/42**, 381–393 (1996).
66. Durose K, Edwards P, Halliday D, *J. Cryst. Growth* **197**, 733–742 (1999).
67. Dobson K, Visoly-Fisher I, Hodes G, Cahen D, *Sol. Energy Mater. Sol. Cells* **62**, 295–325 (2000).
68. Nakayama N *et al.*, *Jpn. J. Appl. Phys.* **15**, 2281 (1976).
69. McCandless B, *Mat. Res. Soc. Symp. Proc.* **668**, H1.6.1–H1.6.12 (2001).
70. Ballif C, Moutinho H, Al-Jassim M, *J. Appl. Phys.* **89**, 1418–1424 (2001).
71. Rogers K *et al.*, *Thin Solid Films*, **339**, 299–304 (1999).
72. Yan Y, Albin D, Al-Jassim M, *Appl. Phys. Lett.* **78**, 171–173 (2001).
73. Nunoue S, Hemmi T, Kato E, *J. Electrochem. Soc.* **137**, 1248–1251 (1990).
74. Martel A *et al.*, *Phys. Status Solidi B* **220**, 261–267 (2000).
75. Dobson K, Visoly-Fisher I, Hodes G, Cahen D, *Adv. Mater.* **13**, 1495–1499 (2001).
76. Wu X *et al.*, *J. Appl. Phys.* **89**, 4564–4569 (2001).
77. Waters D *et al.*, Conf. Rec. 2nd WCPVSEC, 1031–1034 (1998).
78. Oman D *et al.*, *Appl. Phys. Lett.* **67**, 1896–1898 (1995).
79. Rakhshani A, *J. Appl. Phys.* **81**, 7988–7993 (1997).
80. Aspnes D, Arwin H, *J. Vac. Sci. Technol.* **A2**, 1309–1323 (1984).
81. Fisher A *et al.*, *Appl. Phys. Lett.* **70**, 3239–3241 (1997).
82. Grecu D *et al.*, *J. Appl. Phys.* **88**, 2490–2496 (2000).
83. Okamoto T *et al.*, *J. Appl. Phys.* **57**, 3894–3899 (1998).
84. Rose D *et al.*, *Prog. Photovolt.* **7**, 331–340 (1999).
85. Balcioglu A, Ahrenkiel R, Hasoon F, *J. Appl. Phys.* **88**, 7175–7178 (2000).
86. Dobson K *et al.*, *Mat. Res. Soc. Symp. Proc.* **668**, H8.24.1–H8.24.6 (2001).
87. Galloway S, Edwards P, Durose K, *Sol. Energy Mater. Sol. Cells* **57**, 61–74 (1999).
88. Durose K, Edwards P, Halliday D, *J. Cryst. Growth* **197**, 733–740 (1999).
89. Bonnet D, Ed, *Int. J. Solar Energy*, 12, Harwood Academic Publishers, Reading, U.K. (1992).
90. Chu T, Chu S, *Prog. Photovolt.* **1**, 31–32 (1993).
91. Birkmire R, Eser E, *Annu. Rev. Mater. Sci.* **27**, 625–653 (1997).
92. Bonnet D, Meyers P, *J. Mater. Res.* **10**, 2740–2754 (1998).
93. Jackson S, Baron B, Rocheleau R, Russell T, *J. Vac. Sci. Technol. A* **3**, 1916–1920 (1985).
94. Jackson S, Baron B, Rocheleau R, Russell T, *AIChE J.* **33**, 711–721 (1987).
95. Fahrenbruch A, Bube R, Kim D, Lopez-Otero A, *Int. J. Sol. Energy* **12**, 197–222 (1992).
96. McCandless B, Youm I, Birkmire R, *Prog. Photovolt.* **7**, 21–30 (1999).
97. Takamoto T, Agui T, Kurita H, Ohmori M, *Sol. Energy Mater. Sol. Cells* **49**, 219–225 (1997).
98. Tyan Y, Perez-Albuern E, Conf. Rec. 16th IEEE Photovoltaic Specialist Conf., 794–800 (1982).
99. Chu T *et al.*, *IEEE Electron. Dev. Lett.* **13**, 303–304 (1992).
100. Ferekides C *et al.*, *Thin Solid Films* **361–362**, 520–526 (2000).
101. Wu X *et al.*, Conf. Rec. 28th IEEE Photovoltaic Specialist Conf., 470–474 (2000).
102. Ohyama H *et al.*, Conf. Rec. 26th IEEE Photovoltaic Specialist Conf., 343–346 (1997).
103. Bonnet D, Richter H, Jaeger K, Conf. Rec. European 13th Photovoltaic Solar Energy Conversion, 1456–1461 (1995).
104. Bonnet D, Conf. Rec. 14th European Photovoltaic Solar Energy Conversion, 2688–2693 (1997).
105. McCandless B, unpublished work.
106. Powell R *et al.*, U.S. Patent 5,945,163 (1999).

107. Wendt R, Fischer A, Grecu D, Compaan A, *J. Appl. Phys.* **84**, 2920–2925 (1998).
108. Abou-Elfoutouh F, Coutts T, *Int. J. Sol. Energy* **12**, 223–232 (1992).
109. Krüger F, *J. Electrochem. Soc.* **125**, 2028–2034 (1978).
110. Başol B, *J. Appl. Phys.* **55**, 601–603 (1984).
111. Fulop G *et al.*, *Appl. Phys. Lett.* **40**, 327–328 (1982).
112. Bhattacharya R, Rajeshwar K, *J. Electrochem. Soc.* **131**, 2032–2041 (1984).
113. Chu T, Chu S, *Int. J. Sol. Energy* **12**, 122–132 (1992).
114. Sudharsanan R, Rohatgi A, *Sol. Cells* **31**, 143–150 (1991).
115. Jordan J, International Patent Application WO93/14524 (1993).
116. Kester J *et al.*, *AIP Conf. Ser.* **394**, 196 (1996).
117. Ikegami S, Tech. Digest Int'l PVSEC-3, 677–682 (1987).
118. Kim H, Im H, Moon J, *Thin Solid Films* **214**, 207–212 (1992).
119. Clemminck I, Burgelman M, Casteleyn M, Depuydt B, *Int. J. Sol. Energy* **12**, 67–78 (1992).
120. Bauer G, von Roedern B, Conf. Rec. 16th European Photovoltaic Solar Energy Conversion, 173–176 (2000).
121. Jordan J, Albright S, U.S. Patent 5,279,678 (1994).
122. Takamoto T, Agui T, Kurita H, Ohmori M, *Sol. Energy Mater. Sol. Cells* **49**, 219–225 (1997).
123. McCandless B, Birkmire R, Conf. Rec. 28th IEEE Photovoltaic Specialist Conf., 491–494 (2000).
124. Wu X *et al.*, Conf. Rec. 28th IEEE Photovoltaic Specialist Conf., 470–474 (2000).
125. McCandless B, Hegedus S, Conf. Rec. 22nd IEEE Photovoltaic Specialist Conf., 967–972 (1991).
126. Clemminck I *et al.*, Conf. Rec. 22nd IEEE Photovoltaic Specialist Conf., 1114 (1991).
127. Wu X, *J. Appl. Phys.* **89**, 4564–4569 (2001).
128. Meyers P, Leng C, Frey T, U.S. Patent 4,710,589 (1987).
129. McCandless B, Birkmire R, *Sol. Cells* **31**, 527–535 (1990).
130. McCandless B, Hichri H, Hanket G, Birkmire R, Conf. Rec. 25th IEEE Photovoltaic Specialist Conf., 781–785 (1996).
131. Mahathongdy Y, Albin D, Wolden C, Baldwin R, Conf. Rec. 15th NREL PV Rev. Meeting (1998).
132. Zhou T *et al.*, Conf. Rec. 1st WCPVSEC, 103–106 (1994).
133. Qu Y, Meyers P, McCandless B, Conf. Rec. 25th IEEE Photovoltaic Specialist Conf., 1013–1016 (1996).
134. Başol B, Tseng E, Lo D, U.S. Patent 4,548,681 (1984).
135. McCandless B, Moulton L, Birkmire R, *Prog. Photovolt.* **5**, 249–260 (1997).
136. Birkmire R, McCandless B, Shafarman W, *Sol. Cells* **23**, 115–126 (1985).
137. Birkmire R, McCandless B, Hegedus S, *Int. J. Sol. Energy* **12**, 145–154 (1992).
138. Hiltner J, Sites J, *Mat. Res. Soc. Proc.* **668**, H 9.8, 1–7 (2001).
139. Jensen G, Ph.D. Dissertation, Stanford University, Department of Physics (1997).
140. Ohata K, Saraie J, Tanaka T, *Jpn. J. Appl. Phys.* **12**, 1641–1642 (1973).
141. Moon D, Im H, *Powder Metall.* **35**, 53–58 (1992).
142. Jensen D, McCandless B, Birkmire R, *Mat. Res. Soc. Symp. Proc.* **428**, 325–330 (1996).
143. Hill R, Richardson D, *Thin Solid Films* **18**, 25–28 (1973).
144. Compaan A *et al.*, *Mat. Res. Soc. Symp. Proc.* **428**, 367–371 (1996).
145. Bonnet D, *Phys. Stat. Sol.* **A3**, 913–919 (1970).
146. McCandless B, Hanket G, Jensen D, Birkmire R, *J. Vac. Sci. Technol. A* **20**(4), 1462–1467 (2002).
147. Wei S, Zhang S, Zunger A, *J. Appl. Phys.* **87**, 1304–1311 (2000).
148. Ohata K, Saraie J, Tanaka T, *Jpn. J. Appl. Phys.* **12**, 1198–1204 (1973).
149. McCandless B, Engelmann M, Birkmire R, *J. Appl. Phys.* **89**(2), 988–995 (2001).
150. Albright S *et al.*, *AIP Conf. Ser.* **268**, 17–32 (1992).
151. McCandless B, Phillips J, Titus J, Conf. Rec. 2nd WCPVEC, 448–452 (1998).

152. McCandless B, Qu Y, Birkmire R, Conf. Rec. 1st WCPVSEC, 107–110 (1994).
153. Szabo L, Biter W, U. S. Patent 4,735,662 (1988).
154. Albright S, Ackerman B, Jordan J, *IEEE Trans. Elec. Dev.* **37**, 434–437 (1990).
155. Matsumoto H *et al.*, *Sol. Cells* **11**, 367–373 (1984).
156. Lyubormisky I, Rabinal M, Cahen D, *J. Appl. Phys.*, **81**, 6684–6691 (1997).
157. Ringel S, Smith A, MacDougall M, Rohatgi A, *J. Appl. Phys.* **70**, 881–889 (1991).
158. Drayton J *et al.*, Compaan, presented at Spring MRS (San Francisco, April 2001).
159. Romeo N *et al.*, *Sol. Energy Mater. Sol. Cells* **58**, 209–218 (1999).
160. McMahon T, Fahrenbruch A, Conf. Rec. 28th IEEE Photovoltaic Specialist Conf., 539–542 (2001).
161. Sites J, Mauk P, *Sol. Cells* **27**, 411–417 (1989).
162. Kurtz S, Olson J, Kibler A, Conf. Rec. 23rd IEEE Photovoltaic Specialist Conf., 138–141 (1990).
163. Stollwerck G, Sites J, Conf. Rec. 13th European Photovoltaic Solar Energy Conversion, 2020–2022 (1995).
164. Niemegeers A, Burgelman M, *J. Appl. Phys.* **81**, 2881–2886 (1997).
165. McCandless B, Phillips J, Titus J, Conf. Rec. 2nd WCPVSEC, 448–452 (1998).
166. Asher S *et al.*, Conf. Rec. 28th IEEE Photovoltaic Specialist Conf., 479–482 (2000).
167. Fahrenbruch A, *Sol. Cells* **21**, 399–412 (1987).
168. Meyers P, Phillips J, Conf. Rec. 25th IEEE Photovoltaic Specialist Conf., 789–792 (1996).
169. Hiltner J, Sites J, *AIP Conf. Ser.* **462**, 170–173 (1998).
170. Gupta A, Townsend S, Kaydanov V, Ohno T, Conf. Rec. NCPV Rev. Mtg, 271–272 (2000).
171. Hegedus S, McCandless B, Birkmire R, Conf. Rec. 28th IEEE Photovoltaic Specialist Conf., 535–538 (2000).
172. Dobson K, Visoly-Fisher I, Hodes G, Cahen D, *Sol. Energy Mater. Sol. Cells* **62**, 145–154 (2000).
173. Greco D, Compaan A, *Appl. Phys. Lett.* **75**, 36–363 (1999).
174. Stollwerck G, MS Thesis, Colorado State University (1995).
175. Hulstrom R, Bird R, Riordan C, *Sol. Cells* **15**, 365 (1985).
176. Mauk P, Tavakolian H, Sites J, *IEEE Trans. Electron Dev.* **37**, 1065–1068 (1990).
177. Liu X, Sites J, *J. Appl. Phys.* **75**, 577–581 (1994).
178. Scofield J, *Sol. Energy Mater. Sol. Cells* **37**, 217–233 (1995).
179. Phillips J, Birkmire R, McCandless B, Meyers P, Shafarman W, *Phys. Stat. Sol. (b)* **194**, 31–39 (1996).
180. Matulionis I, Nakada S, Compaan A, Conf. Rec. 26th IEEE Photovoltaic Specialist Conf., 491–494 (1997).
181. Willing F *et al.*, Conf. Rec. 21st IEEE Photovoltaic Solar Energy Conversion, 1432–1436 (1990).
182. van den Berg R *et al.*, *Sol. Energy Mater. Sol. Cells* **31**, 253–261 (1993).
183. *Kirk-Othmer Encyclopedia of Chemical Technology*, Third Edition, Vol. 11, 807–880, John Wiley and Sons, Inc., New York (1980).
184. Brown R, U.S. Geological Survey Minerals Yearbook, (2000) U.S.G.S., 67.1–67.4.
185. Andersson B, *Prog. Photovolt. Res. Appl.* **8**, 61–76 (2000).
186. Gerhardinger P, McCurdy R, *Mat. Res. Soc. Symp. Proc.* **426**, 399–410 (1996).
187. Zweibel K, *Sol. Energy Mater. Sol. Cells* **59**, 1–18 (1999).
188. Maycock P (Ed), *Photovoltaic News*, **20** (Feb, 2001).
189. Green M *et al.*, *Prog. Photovolt. Res. Appl.* **7**, 31–37 (1999).
190. Suyama N *et al.*, Conf. Rec. 21st IEEE Photovoltaic Specialist Conf., 498–503 (1990).
191. Rose D *et al.*, Conf. Rec. 28th IEEE Photovoltaic Specialist Conf., 428–431 (2000).
192. Cunningham D *et al.*, Conf. Rec. 16th European Photovoltaic Solar Energy Conversion, 281–285 (2000).
193. Fan J, Palm B, *Sol. Cells* **11**, 247–261 (1984).

194. Nell M, Barnett A, *IEEE Trans. Elec. Dev.* **ED-34**, 257–265 (1987).
195. Basol B, Kapur V, Kullberg R, Conf. Rec. 20th IEEE Photovoltaic Specialist Conf., 1500–1504 (1988).
196. Rohatgi A, Sudharsanan R, Ringel S, MacDougal M, *Sol. Cells* **30**, 109–122 (1991).
197. Romeo A, Batzner D, Zogg H, Tiwari A, *Mat. Res. Soc. Symp. Proc.* **668**, H3.3.1–H3.3.6 (2001).
198. Zweibel K, Conf. Rec. IECEC (Denver, CO, 1988).
199. Charlton D, *J. Cryst. Growth* **59**, 98–110 (1982).
200. Li T, Conf. Rec. 33rd Electronic Components Conference, 546–551 (1983).
201. Niraula M *et al.*, *Appl. Phys. Lett.* **75**, 2322–2324 (1999).
202. Fthenakis V, Eberspacher C, Moskowitz P, *Prog. Photovolt.: Res. Appl.* **4**, 447–456 (1996).
203. Zweibel K, Moskowitz P, Fthenakis V, NREL Technical Report 520–24057 (Feb. 1998).
204. Herndon M, Gupta A, Kaydanov V, Collins R, *Appl. Phys. Lett.* **75**, 3503–3506 (1999).
205. Gessert T, Duda A, Asher S, Narayanswamy C, Rose D, Conf. Rec. 28th IEEE Photovoltaic Specialist Conf., 654–657 (2000).